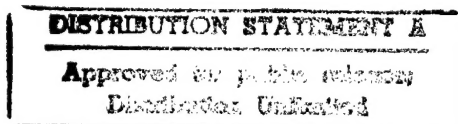JPRS-CST-86-042

2 OCTOBER 1986

China Report

SCIENCE AND TECHNOLOGY

DTIC QUALITY INSPECTED 4

19981021 089

FBIS FOREIGN BROADCAST INFORMATION SERVICE

1
76
A05

CHINA REPORT

SCIENCE AND TECHNOLOGY

CONTENTS

PEOPLE'S REPUBLIC OF CHINA

ABSTRACTS

/7310

NATIONAL DEVELOPMENTS

SYSTEMATIZED MICROCOMPUTER NOMENCLATURE INTRODUCED

Beijing WUXIANDIAN [RADIO] in Chinese No 4, 11 Apr 86 p 8

[Article by Qian Dongjun [6929 2639 6511]: "Nomenclature for Chinese-Made Microcomputers"]

[Text] In the wake of the development of China's computer industry, product series and types of Chinese-made computers have been increasing rapidly. To enable readers to understand these computer series and models, here is a brief introduction on how the Computer Industrial Administration Bureau names these computers.

The nomenclature pattern consists of three parts, i.e., code name or trade name of the enterprise; a 4-digit number; and a suffix as shown in the figure.

Enterprise code or Trademark	0	x	x	x	Suffix
(1)	(2)	(3)	(4)	(5)	(6)

(1) Enterprise code name or trade name:

There is no uniformity in manufacturers' code names or trade names. For example, "Changchen" [Great Wall], "Zijin" ["Purple Gold", "TQ"; "DJS", etc.

(2) Computer series number:

It is expressed from $0 \sim 9$, in which "0" indicates the microcomputer series. The other numbers represent minicomputers series or large-, and medium-size computer series.

(3) System classification number:

This numeral here pertains to the type of central processing unit (CPU) and is expressed as follows:

```
    1 --------------- bit machine;
    2 --------------- 4-bit machine;
    3 --------------- 6502 CPU;
    4 --------------- Z80/Z8000 CPU;
    5 --------------- 8080/8086 CPU (including 8085; 8088);
and 6 --------------- 6800/68000 CPU (including 6809).
```

(4) Microcomputer series type expressed in numerals:

```
    0 --------------- singleboard machine;
    1 --------------- 8-bit personal machine;
    2 --------------- quasi 16-bit personal machine;
    3 --------------- 16-bit personal machine;
    4 --------------- 32-bit personal machine;
    5 --------------- 8-bit bus structured microcomputer;
    6 --------------- quasi 16-bit bus structured microcomputer;
    7 --------------- 16-bit bus structured microcomputer;
    8 --------------- 32-bit bus structured microcomputer;
and 9 --------------- other types of microcomputer.
```

(5) Microcomputer bus types expressed in numerals:

```
    0 --------------- not bus organized structure, such as the personal
                      computer, singleboard machine, etc.;
    1 --------------- S-100 bus;
    2 --------------- multiple bus (MULTIBUS);
and 4 --------------- other bus types.
```

(6) Suffix:

This part is used selectively and is not yet standardized. It is denoted by a letter or numeral to differentiate the product-number of performance capability.

The aforementioned standardization is suited for the state priority microcomputer series. As for the non-state priority series, console type computers and pocket type computers, are all named by individual enterprise units.

The following example of a Chinese-made computer using this nomenclature method illustrates a quick assessment of the domestic product.

```
           (1)        (2)   (3)  (4)  (5)  (6)
        Great Wall     0     5    2    0    A
                                              └─→ A grade product
                                         └────→ non-bus type structure
                                    └─────────→ quasi 16-bit personal computer
                               └──────────────→ 8086 CPU
                          └────────────────────→ microcomputer
                  └──────────────────────────→ brand
```

PHYSICAL SCIENCES

SEA-AIR HEAT EXCH/ .GE OVER NORTH PACIFIC

[Article by Zhao Yongping [6392 3057 1627], Institute of Oceanology, Chinese
Academy of Sciences, Qingdao: "A Preliminary Study on the Influence of Sea-air
Heat Exchange in tne Mid-latitude of the North Pacific on the Atmospheric Cir-
culation There," Contribution No 1264 from the Institute of Oceanology, Chinese
Academy of Sciences, paper received on: 25 November 1983]

[Text] English Abstract: Characteristics of the sea-air heat exchange in the
mid-latitude of the North Pacific showed that there was a good relationship
between the sea-air heat exchange on the Kuroshio and the long wave over the
North Pacific and ᴄhat the strength of the cold air made a great contribution
to the sea-air heat exchange, which might be a more effective factor for pre-
diction than the air or sea temperature alone. Based upon the analysis, a sim-
ple irreversible ᴍᴏᴅel was proposed: the stronger (weaker) the cold air, the
bigger (smaller) the sea-air heat exchange, the more improvement in the longi-
tudinal (latitudiᴎᴀl) circulation, the stronger (weaker) the cold air, ...
This process generally began in the late autumn and continued till the adjust-
ment of the circulᴀtion in the summer half year.

In recent years there have been great advances in research on sea-air interac-
tion, with specially clear results in research on interaction between low lati-
tude equatorial seas and atmospheric circulation. The expanse of mid-latitude
sea surface, especially the warm northward currents at the western border of
the ocean, carry the heat radiated by the sun and absorbed by the ocean at low
latitudes to mid-high latitude seas, and through the sea-air interface, the seas
transfer heat to the atmosphere all year. Research shows that the abnormalities
of the sea-air heat exchange in these sea areas has a definite influence on the
atmosphere. But ʰ w great is the influence of the mid-latitude seas on the
atmosphere? By what kind of process does this influence take place? These
questions have not yet been researched in detail, and the results of work that
has already been done are not uniform[1,4]. This paper is an attempt to
explore the facts ᴏf the interrelationship between mid-latitude sea-air heat
exchange and the atmospheric circulation in the air above it and to discuss the
process of the possible influences between them.

I. Characteristics of Sea-Air Heat Exchange in the Mid-Latitudes of the North Pacific

Using average hydrometeorological data for many years Wyrtki[5] calculated the average heat-air exchange distribution for the entire Pacific Ocean and pointed out that the greatest sea to atmosphere heat transfer area was along the axis of the Kuroshio. We have calculated the values of sea-air latent heat and sensible heat exchange at 35°N, 130°E-130°W and graphed them in Figure 1 to explain the latitude distribution of sea-air heat exchange. From the graph it can be seen that the average annual heat transfer to the atmosphere is the greatest in the western part of the Pacific, especially in the area of the Kuroshio, with a total heat transfer (a combination of latent heat and sensible heat) which reached 400 cal/cm^2.d, with the maximum at 140°E rapidly diminishing towards the east, and becoming very small in latitudes east of 180°. The average total transfer is approximately 150 cal/cm^2.d. The average heat transfer of the western seas is approximately three-times that of the eastern part.
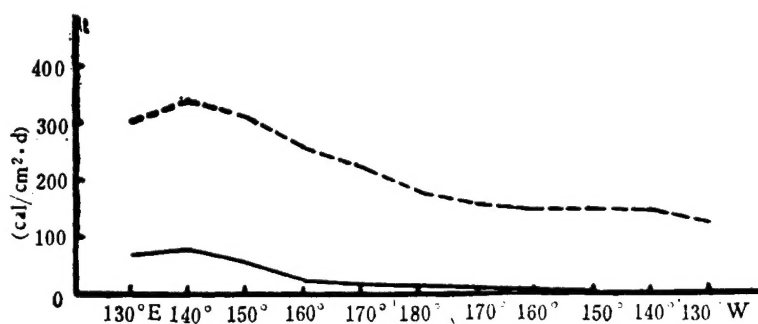

Figure 1   Latitudinal Distribution of Sea-Air Heat Exchange in the Mid-latitudes of the North Pacific (cal/cm^2.d)

--------- Latent Heat;   _____ Sensible Heat

The annual changes in the sea-air heat exchange (sensible heat) of the western and eastern parts of the mid-latitudes of the North Pacific are illustrated in Figure 2. In the figure, 33°N, 140°E and the buoy station N (30°N, 140°W) represent the changes in sea-air heat exchange in the western and eastern parts of the ocean, respectively. From the figure it can be seen that there is a trend in annual changes between the two, with the winter the maximum and the summer the minimum, but the extremes of the annual changes in the two are not the same. In the western part of the North Pacific, the sea gives the most heat to the atmosphere in winter, with a value of about 320 cal/cm^2·. In the summer, the sea obtains heat from the atmosphere, with a value of 10 cal/cm^2.d, for an annual range of 330 cal/cm^2.d. The sea in the eastern part of the North Pacific transfers heat to the atmosphere all year, with a maximum summer value of 324 cal/cm^2.d, and a summer minimum of 127 cal/cm^2.d, for an annual range of 200 cal/cm^2.d, the former being 2.5 times the latter.
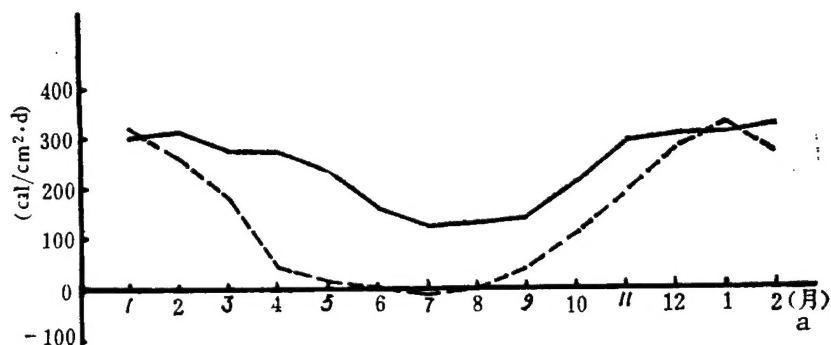
4

Figure 2   Annual Changes in Sea-Air Heat Exchange in Western and
Eastern Parts of the North Pacific (cal/cm^2.d)

--------- Latent Heat;   _____ Sensible Heat

Key: a.   Month

Summarizing the above, we can tell that the western sea region (primarily the Kuroshio warm current region) occupies a very important place in the mid-latitude seas sea-air heat exchange in the North Pacific since the volume of sea-air heat exchange in this region and the annual changes are much greater than in the eastern seas. It can be predicted that the abnormality in the sea-air heat exchange in this region can have an important influence on mid-latitude atmospheric circulation.

II. Influence of Sea-Air Heat exchange in the Mid-latitudes of the North Pacific on Air Circulation Above It

After calculating the sea-air heat exchange values for the western part of the North Pacific by month for the 114 months between July 1963 and December 1972, we calculated the average values for the 10 stations at 21°N, 125°E; 25°N, 125°E; 29°N, 130°E; 30°N, 135°E, 33°N, 140°E; 33°N, 145°E; 35°N, 150°E; 37°N, 155°N, 160°E; 37°N, 165°E. These stations are in the vicinity of the axis of the Kuroshio current, and the changes in their average values can represent the characteristics of sea-air heat exchange in the western seas. Because the sensible heat values are rather small, especially in the summer, the latent heat transfer values (Q_E) were adopted to represent the total sea-air heat exchange of this sea region. To eliminate annual changes, we subtracted the multi-year average values of the months from the month by month latent heat values calculated and arrived at anomalous values month by month. To eliminate small perturbations, we also carried out running averages for 5 months on the data.

For the characteristics of atmospheric circulation above the North Pacific we indicated it by using the air latitudinal circulation coefficient of this area, taking 25°N, 50°N, 140°E-140°W, and the 500mb altitude (h) at each 10° longitude calculated according to the following equation

5

$$I_z = \sum_{i=1}^{9} h_{\varphi_{25}} - \sum_{i=1}^{9} h_{\varphi_{50}}$$

Since Pacific air observation data is sparse, we discovered in some of the calculation results that the time sequences of latitudinal circulation coefficient for some months was very irregular, clearly these are caused by data errors. To eliminate the errors, we first of all plotted the circulation coefficients we had calculated, and on the basis of the continuity of the circulation after carrying out regularized corrections of the data, then carried out anomalous sliding. Thus we obtained filtered annnual changes and anomalies of small perturbations of less than 5 successive months.

The above results are plotted in Figure 3. From the figure it can be seen that the two exhibit a clear negative correlation; the correlation coefficient is -0.45. The number of sequential samples in this data was N=114, and the confidence of this correlation is far beyond 0.001. That is, in tl mid-latitudes of the western part of the North Pacific, when a greater than normal amount of heat is transferred from the sea to the atmosphere, the latitudinal circulation index above the Pacific Ocean becomes weaker. This means that the longitudinal direction of the atmospheric long waves increases, and a ridge develops; conversely, when a less than normal amount of heat is transferred from the sea to the atmosphere, the latitudinal circulation index above the Pacific Ocean becomes stronger, and at this time the west wind intensifies and the atmospheric long waves are shallow.
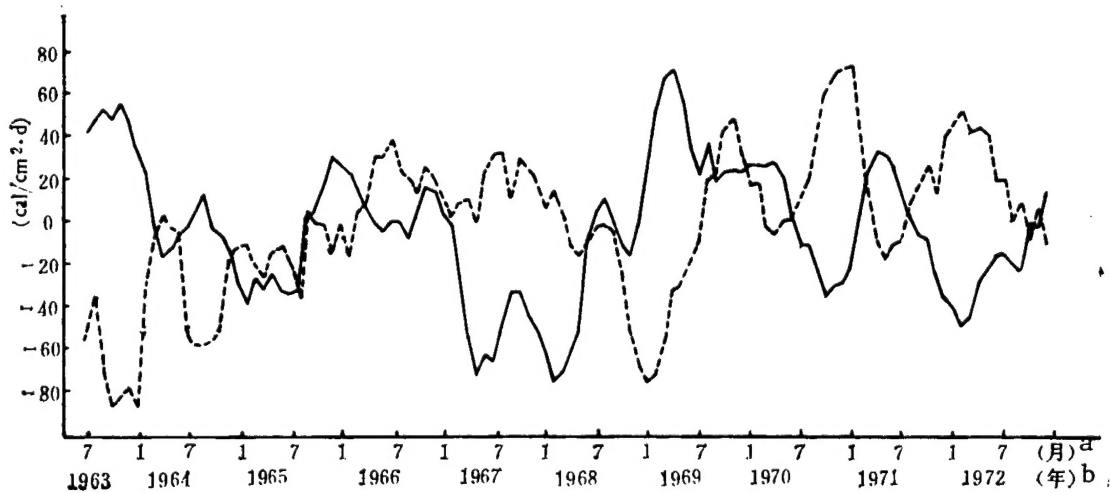

Figure 3 Development Curve of the Sea-Air Heat Exchange Anomalous Value (cal/cm^2.d) and Anomalous Value of the Latitudinal Circulation Indicator (Geopotential Shi Meters) of Mid-Latitudes of the Western Part of the North Pacific

--------- Sea-Air Heat Exchange;   _____ Latitude Circulation Indicator

Key: a. Month   b. Year

6

To understand the interaction process of the sea and the atmosphere, we also calculated the time lag correlation of the two (Figure 4). Zero on the horizontal axis is the synchronous correlation of the two, greater than zero is the correlation of latent heat on atmospheric circulation in a later period, smaller than zero is the correlation of earlier period circulation on latent heat. The vertical axis is the absolute value of the correlation coefficient, the broken line parallel to the horizontal axis is the critical degree of confidence value 0.001 (r=0.32). From the figure it can be seen that the synchronous correlation of the two is best (r=-.045). The correlation of the atmospheric flow of the preceding 1-2 months with regard to the latest heat for that month and that month's latent heat with regard to the atmospheric flow of following 1-2 months exceeded a degree of confidence of 0.001. This result indicates how much the atmospheric circulation of the preceding 1-2 months and the current month influences the sea-air heat transfer of that month and how much of the sea-air exchange of that month influences the atmospheric circulation of that month and the following 1-2 months, the two are in a negative correlation.
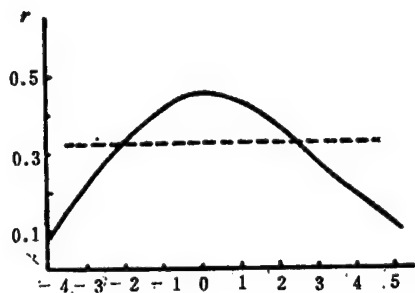

Figure 4 Time Lag Correlation of Sea-Air Heat Exchange and Latitudinal Circulation Indicator (Dashed Line in the Figure is the 0.001 Degree of Confidence Line)

To explain further the circulation characteristics of the abnormal heat time, we selected two typical months, in which the latitudinal circulation indicator of November 1963 was a large zhengjunian [2973 6415 1628] and the sea-air heat transfer was a large funjunian [6298 6415 1628]; but November 1970 was the reverse, the latitudinal circulation indicator was a large funjunian and the sea-air transfer was a large zhengjunian. For the warming above the seas in these 2 months see Figure 5. From the figure it can be seen that in November 1963 along the Kuroshio there is a belt of high values, with the maximum above 600 cal/cm². In November, 1970, along the Kuroshio there is also a belt of high values, but the maximum is above 1,000 cal/cm², far greater than the value for November, 1963. Figure 6 is a 500mb vorticity field of the same period. For November, 1963, the vorticity field exhibits a latitudinal distribution. Above 45°N is a positive vorticity area and south of 45°N is a negative vorticity area. This indicates that in this month, the circulation regular, and the west wind is strong. In November 1970, the primary characteristic of the vorticity field is the longitudinal distribution of the vorticity. Negative vorticity in the central Pacific clearly extends towards the north, and the two sides are positive vorticity, this indicates that at this time, the longitudinal direction of the atmospheric circulation is great, and the high ridge in the central Pacific rises towards the north.

7

Figure 5   Warming Field Above the Western Part of the North Pacific
in November, 1963 (a) and November, 1970 (b) (cal/cm²·d)

Figure 6   500mb Vorticity above the North Pacific in November, 1963 (a)
and November, 1970 (b)

The above facts show that the mid-latitudinal seas in the central part of the
North Pacific have a clear influence on the atmospheric circulation in the air
above it.   When the heat received by the sea is greater than in normal years,
the latitudinal circulation indicator of the air above the North Pacific
diminishes, and the longitudinal nature of the circulation increases.   When
the sea receives less heat than in a normal year, the latitudinal circulation
indicator of the air above the North Pacific increases and circulation is
smooth.

8

III. Discussion

Below is a preliminary discussion of the characteristics and process of sea-air interaction in the mid-latitude seas.

1. Characteristics of Mid-latitude Sea Sea-air Interaction

Sea-air interaction is primarily carried out through sea-air heat exchange. Existing researches show that in equatorial seas, changes in water temperature make a large contribution to sea-air heat exchange in that region. El Nino is a characteristic in which the rise in water temperature is primary. This water temperature abnormality leads to changes in woke [3087 0344 Walker?] circulation. Kraus[4] pointed out that the contribution of water temperature to sea-air heat exchange increases as the latitude decreases. The author[1] has also pointed out that the sea-air heat exchange in the eastern sea in the winter is primarily determined by the strength or weakness of the cold air, and the contribution of water temperature is secondary. This article further calculated the relationship of the month to month heat exchange and water temperature, air temperature and wind speed for stations at 33°N,135°E, 33°N,150°E, and 33°N,165°E, and using the average correlation of these three stations as representative further discussed the characteristics of mid-latitude seas sea-air heat exchange.

Table 1 Average Correlation of Sea-Air Sensible Heat and Meteorological Factors at Stations at 33°N,135°E, 33°N,150°E, and 30°N,165°E (N=14)

item 项	month 月 r	1	2	3	4	5	6	7	8	9	10	11	12
$Q_c - T_a$		−0.70	−0.82	−0.75	−0.33	−0.62	−0.64	−0.23	−0.40	−0.75	−0.50	−0.72	−0.90
$Q_c - T_w$		0.29	0.07	0.10	−0.32	0.06	−0.28	0.24	0.45	0.20	0.22	0.18	−0.02
$Q_c - v$		0.37	0.32	0.55	0.16	0.39	−0.13	−0.20	−0.05	0.34	0.33	0.55	0.39

Taking 0.01 as the standard of confidence, it can be seen from Table 1 that the correlation of sea-air heat exchange and air temperature is closest during November to March, and in the other months it deviates, although for individual months the correlation is good, the time is not continuous; there is no correlation between the months' sensible heat exchange and the water temperature and wind speed. There is also a type of relationship between latent heat transfer and meteorological factors. This result indicates that in mid-latitude seas, in the winter months (mainly November through march) the strength of northern cold air makes a decisive contribution to sea-air heat exchange. Actually, the sea-air heat exchange in mid-latitude seas is an important cause of changes in surface layer water temperature. Jacobs[3] made sea surface sea-air heat exchange an important upper boundary conditions of changes in water temperature for forecasting water temperature. In the summer months (April through October) meteorological factors do not make a big contribution to sea-air heat exchange, and it can be accepted that in this time period, sea-air heat exchange is the

result of the combined action of meteorological factors. Clearly, this is not the same as the characteristics of sea-air heat exchange is low latitude seas.

Summing up the above, in changes in sea-air heat exchange in mid-latitude seas, the strength of the cold air has an unusually important contribution, especially in the winter. When discussing the influence of mid-latitude seas on the atmosphere, sea-air heat exchange should be considered as a basic factor.

2. The Influence Of Sea-Air Heat Exchange On Atmospheric Circulation Above the North Pacific

The area of the Kuroshio is in the vicinity of the long wave ridge in the Pacific. According to long wave theory, when there is abnormally high warming in front of the ridge, it is favorable for developing low layer cyclones and high air high pressure ridge in front of the ridge. Conversely, when there is abnormally low warming in front of the ridge, it is not favorable for the development of high air high pressure ridge in front of the ridge. Since the large circulation changes in the west wind zone is a process of destroying and establishing latitudinal circulation, the strength of the latitudinal circulation indicator reflects this change. When a ridge develops in the west wind zone the latitudinal circulation indicator diminishes; when the circulation in the west wind zone is regular, the latitudinal circulation indicator increases. Thus, we can explain from a theoretical perspective, the negative correlation of sea-air heat exchange in the mid-latitude seas of the western part of the Northern Pacific and circulation over the Northern Pacific, i.e., when the sea-air heat exchange is great (little), then the latitudinal circulation indicator is small (large).

This paper further explains this process using the 500 mb altitude field and corresponding sea-surface air pressure field of November 1963 and November 1970. Figure 7 is the 500 mb altitude anomalous field situation and comparing the distribution in November 1963 and November 1970, one can see clearly that when the sea-air heat exchange is less than in a normal year (November, 1963) the western and central part of the North Pacific is positive anomalous with its maximum value at 9 geopotential shi [0087] meters, the eastern part is negative anomalous, with its maximum at -12 geopotential shi meters; when the sea-air heat transfer is greater than in a normal year (November, 1970), the central and eastern parts of the North Pacific is greatly positive anomalous with a maximum value of +19 geopotential shi meters, and the western part is negative anomalous with a maximum value of -18 geopotential shi meters. The distribution of these two anomalous fields indicates that the circulation of the former (west positive and east negative) is smooth and the longitudinal degree of circulation of the latter (west negative and east positive) becomes greater, becoming stronger in the high pressure ridge in the central and eastern parts of the Pacific. Figure 8 is the corresponding sea surface air pressure field. Con_ - ing the two, we note the following differences: in November, 1963, low pressure was continuous from central Pacific to the North American continent, indicating that cyclone exhibited primarily latitudinal activity; in November, 1970, the longitudinal activity of the cyclone increased, and at this time the continental cold high pressure was also stronger than the cold high pressure of November, 1963; in November, 1963 the secondary high ridge line tended south; in November,

10

1970, the secondary high ridge position was inclined north. Clearly these distributions correspond one-for-one with the 500 mb altitude field situation.
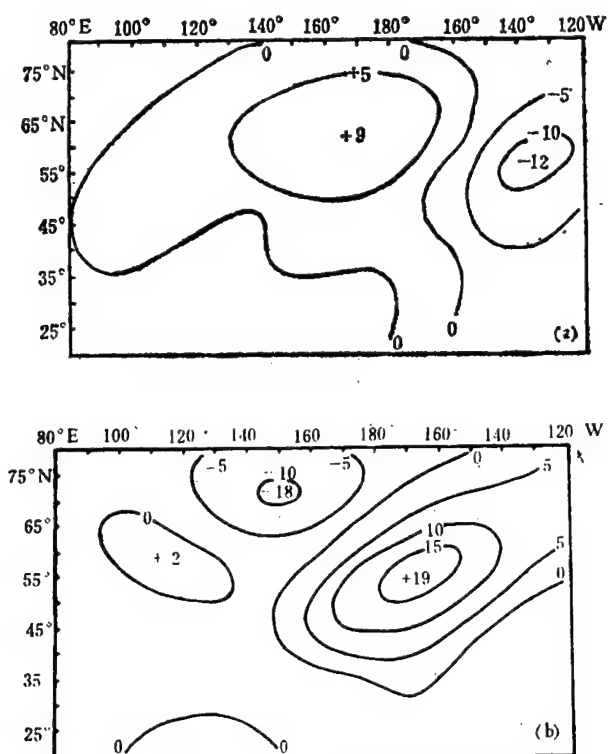
Figure 7   Anomalous Field at 500mb Altitude in November, 1963 (a)
           and November, 1970 (b) (Geopotential Shi Meters)
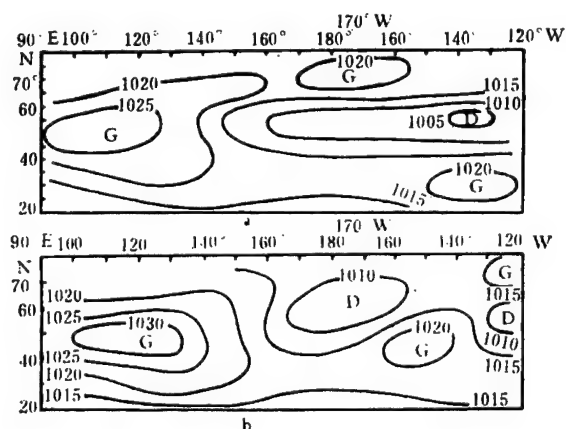
Figure 8   Sea Surface Atmospheric Pressure Field in November, 1963 (a)
           and November, 1970 (b)

From this we can draw the conclusion that abnormalities in heat fields received by the seas clearly have an impact on atmospheric circulation. When the sea-air heat exchange in the Kuroshio seas is greater (lesser) than in normal years, the non-adiabatic heat obtained by the atmosphere is greater (lesser) than a normal year, it heats up, promoting the development (weakening) of a North Pacific high pressure ridge, and corresponding changes occur in the sea-surface air pressure field also changes due to this.

There has been much research on the question of the time lag of sea-air interaction, but the results are still not uniform. Namias holds that there is a clear seasonal time lag between North Pacific atmosphere and the sea; Kraus holds that if the time lag is too long, it cannot produce resonance between the sea and the air and weakens the interaction. Bjerknes also points out that the time lag between large-scale atmospheric circulation and initial abnormalities of equatorial marine heat transfer are very small and can be calculated daily. The calculation results of this paper show (Figure 4) that correlation between the sea-air heat exchange and latitudinal circulation of a particular month are the closest and that there is a clear influence of the sea-air heat exchange of a particular month on the circulation of the succeeding 1-2 months and of the circulation of the preceding 1-2 months on the sea-air heat exchange of that month. This phenomenon where the correlation of the same period is best may also be another feature of mid-latitude sea-air interaction. As far as the causality of its interaction, one can imagine that a specific west wind circulation field first of all determined the sea-air heat exchange field, and once the atmosphere had obtained an abnormal sea heat transfer, the original circulation circumstances would be strengthened and maintained, and then the two would constantly interact.

From Figure 3 it can be seen that once the heat exchange field or latitudinal circulation field have been established, they can frequently be maintained for a long time. Between 1963 and 1972 a total of 12 exchange processes took place, of which 8 were as long as 6 months and 4 were as long as 10 months, with the longest being 25 months. Adding up the exchange periods, most occurred in the summer (10/12), while only 2 occurred during the early winter (December). Under ordinary circumstances, the longitudinality of the west wind-borne long wave in the North Pacific is favorable to strengthening the southward trend of the cold air; conversely, if the cold air position tends northward, the strength weakens. From this we can tell that in the winter half-year, when cold air is colder (warmer) than in a normal year, it creates an abnormal strength (weakness) in the heat exchange in that part of the sea increasing (decreasing) and maintaining the low (high) indicator of the corresponding latitudinal circulation] the longitudinality of the long wave in the air above the Northern Pacific. This situation also further benefits the increasing (decreasing) southward movement of cold air and thus forms an irreversible process. Once this process is established, it can be maintained for a long time. In the summer half-year, due to exchanges which occur in the circulation field, sea-air heat exchange also changes with them. Once a new circulation field is established, a new round of irreversible processes begins immediately between the sea-air heat exchange in the Northern Pacific and the atmospheric circulation in the air above it. Since this is an irreversible regenerative action, there must be a good correlation between a month's sea-air heat exchange with regard

12

to the circulation field of the following month and the circulation field of the preceding month with regard to the sea-air heat exchange field of that month. Thus explaining fact that the correlation of the preceding and succeeding months in Figure 4 has a high degree of confidence.

Summarizing the Above, we get a simple irreversible model of the interaction of the mid-latitude seas of the North Pacific and the atmospheric circulation above it, i.e., cold air strength (weakness)-->the sea transmits much (little) heat to the atmosphere-->the Pacific Ocean's long wave high pressure ridge intensifies (weakens) and longitudinal (latitudinal) circulation intensifies and is maintained-->cold air intensifies (weakens)-->the sea transmits much (little) heat to the atmosphere-->... Generally speaking, the length of the period of maintenance is determined by the adjustment of the summer half year circulation field.

IV. Brief Conclusion

1. Year-round heat transfer to the atmosphere in the mid-latitudes of the Northern Pacific is clearly greater in the western part than in the eastern part; annual changes in heat exchange is clearer in the western part than in the eastern part; strength of winter cold air determines the extent of sea-air heat exchange.

2. Sea-air heat exchange in the mid-latitudes of the western part of the North Pacific clearly influences the atmospheric circulation above the North Pacific. When a greater amount of heat is transferred to the atmosphere than in a normal year in these seas, the Pacific Ocean high pressure ridge weakens, and latitudinal circulation intensifies. The maintenance of this process is closely related to abnormal sea surface non-adiatic heating.

3. Mid-latitude sea sea-air interaction is an irreversible process which is determined by the strength of the cold air of the winter months. When the cold air strengthens (weakens) the sea-air heat exchange strengths (weakens), and the development of the long-wave ridge above the Pacific Ocean is strengthened (weakened). These results also on the other hand promote the continued strength (weakness) of the cold air. It continues this way uninterruptedly until the summer months (April-October) circulation is adjusted.

The changes in circulation caused by the west wind are created by a variety of factors and the sea-air heat exchange of the low latitude seas also has an important impact on the mid-latitude circulation. Thus, low-latitude seas should be considered as a research topic in itself. In addition, the irreversible process of mid-latitude seas sea-air interaction and under what conditions the exchange occurs and can be maintained are also key questions in long range forecasting. We should carry out further research and exploration on these topics.

13

REFERENCES

1. Zhao Yongping [6392 3057 1627], Zhang Bicheng [1728 1801 2052], Jing Licai [0064 4539 2088], 1983. DONGHAI HECHAI HAI-QI RELIANG JIAOHUAN DUI CHANG-JIANG ZHONG-XIA YOU XUNGQI JIANGSHUIDE YINGXIANG [INFLUENCE ON EASTERN SEA KUROSHIO SEA-AIR HEAT EXCHANGE ON THE FLOOD STAGE PRECIPITATION ON THE MID- AND LOWER REACHES OF THE CHANGJIANG], Haiyang Yu Chaozhao [Oceanlogica et Limnologica Sinica], 14(3): 256-262.

2. Pan Yihang [3382 0110 5300], 1975. DONG-CHUN HAIYANG JIARECHANG YU LIANGHU PENDI XUNQI JIANGSHUIDE CHUBU FENXI [ANALYSIS OF WINTER-SPRING OCEAN WARMING FIELDS AND PRECIPITATION DURING THE FLOOD PERIOD IN THE TWO LAKE BASINS], Zhongguo Kexueyuan Daqi Wuliso Jikan [Publication of the Atmospheric Physics Institute of the Chinese Academy of Sciences], 6:102-115.

3. Jacobs, J., 1967. NUMERICAL SEMIPREDICTION OF MONTHLY MEAN SEA SURFACE TEMPERATURE, J.G.R. 172 (6): 1681-1689.

4. Kraus, B., 1972. THREE-DIMENSION INTERACTIONS. ATMOSPHERE-OCEAN INTERACTION, PART 7, Oxford University Press, pp 200-254.

5. Wyrtki, K., 1965. THE AVERAGE ANNUAL HEAT BALANCE OF THE PACIFIC OCEAN AND ITS RELATION TO OCEAN CIRCULATION. J.G.R. 170(18):4547-4559.

APPLIED SCIENCES

OPTIMUM OUTPUT POWER OF SELF-SUSTAINED DISCHARGE TRANSVERSE FLOW CO$_2$ LASER

[Article by Chu Zexiang [2806 3419 3276], Chen Liyin [7115 7787 0692], and
Wu Zhongxiang [0702 0022 4382] of the Institute of Mechanics, Chinese Academy
of Sciences]

[Text] Abstract: The output power of a transverse flow CO$_2$ laser is studied
as a function of the shape of the discharge zone, the position of the cavity,
the size and coupling of the mirrors and the velocity of the gas flow. The
trends obtained are useful for experimental research and laser design.

I. Introduction

Kopferman[1] used the simple discharge model of Condon and Shortley[2] to calcu-
late the saturation gain and output power of a transverse flow CO$_2$ laser.
He obtained a simple scheme for computing the output power of a quasi-two-
dimensional transverse flow electrically excited CO$_2$ laser. Using this
scheme we studied the effects of the shape of the discharge zone, the posi-
tion of the cavity, the size and coupling of the mirrors and the velocity of
the gas flow on the output power.

Figure 1 shows the setup schematically. The metal plate ABCD is the anode,
plate EFGK is the cathode (the cathode can have a tubular, plate, or needle
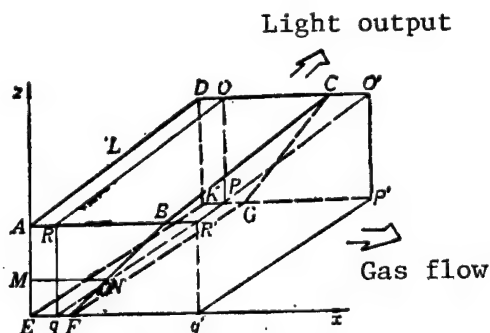geometry), and the electrode separation is AE = H.

Figure 1. Transverse flow self-sustained discharge CO$_2$ laser
           Anode--ABCD, AB = a; Cathode--EFGK, EF = b

If the electron density n_e in the excitation zone is uniform along the x direction but may vary in the z direction, then,

$$n_e = \frac{J}{L \cdot f(z) \cdot e \cdot \nu_D}$$

(1)

where J is the total current, L is the cavity length, ν_D is the drift velocity, e is the electron charge, and

$$f(z) = \left[b + \frac{(a-b)}{H} z \right]$$

(2)

in which z is the width of the excitation zone, and a = AB, b = EF are respectively the X direction dimension of the anode and the cathode. The CO_2, N_2 and H_e gas mixture flows in through the AEKD plane. Cavity mirrors OO'P'P and qq'R'R are placed perpendicular to both the gas flow and the electric field. The reflection coefficients are respectively R_1 and R_2.

Following the approach of Ref. 1, we solve simultaneously the conservation equation and the relaxation equation of an ideal one-dimensional gas for a fixed height z to obtain the one-dimensional distribution of the field strength, the saturation gain, and the gas parameter for the layer z. From the calculation results for different z, we obtain the quasi-two-dimensional distribution in the xz plane caused by the electron density differences in the layers. For the relaxation model we still use the three vibration mode system. As can be seen from Eq. (1), for a triangular or trapezoidal excitation region, the electron density n_e in the cavity will change with the height z and so will the light intensity I. In order to evaluate the effects of the shape of the excitation region on the light intensity, we estimate the output power of a layer at height z and take the intensity I to be a constant in the x direction. This is equivalent to slicing the cavity in the z direction. For each layer the stable oscillation condition of the cavity[1] is:

$$\int_0^w G\,dx = -\frac{w}{2L} \ln(R_1 R_2)$$

(3)

where w is the width of the mirror. This equation describes the gain and loss relationship for a radiation field moving in the gas flow direction in the cavity.

II. Calculation Results and Analysis

Typical conditions used in the calculation are: initial temperature $T_0 = 293$ K, initial velocity $u_0 = 70$ m/s, initial pressure $P_0 = 20$ Torr, $\psi_{CO_2}:\psi_{N_2}:\psi_{He} = 5:27:68$, and $E/N = 2.2 \times 10^{-10}$ V·cm².

1. Effects of the shape of the discharge zone

Figure 2 shows the z dependence of the light intensity for a triangular (AB = 10 cm) and a trapezoidal (AB = 8 cm, EF = 3 cm) discharge zone with the front edge of a 5 cm long 3 cm high mirror at 1 cm from the gas inlet.

16

As can be seen, the light intensity of triangular discharge zone has a
stronger z dependence. This may be explained by the dependence of the
electron density on the height z and on the shape of the discharge zone.
Equation (2) shows that n_e and f(z) are inversely proportional; the narrower
the greater the n_e. However, since f(z) is directly proportional to z, the
z dependence of the electron density and the light intensity is stronger.
For a trapezoidal discharge zone, b $\neq$ 0 and the z dependence of f(z) is
relatively flat. If the discharge zone is rectangular (AB = EF), then n_e is
a constant in the z direction and the light intensity will not vary with
height. But since E/N increases slightly in the x direction (E is the field
intensity and N is the total number of particles per unit volume), the power
will increase. From the calculated results, this was found to be a 10 per-
cent effect.
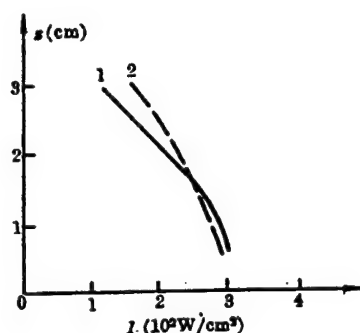

Figure 2.   Effects of the shape of the discharge zone on the
            light intensity
            Curve 1--Triangular zone; Curve 2--Trapezoidal zone

For the conditions investigated in this work, a higher n_e leads to a higher
light intensity and output power. Therefore, increasing n_e by suitably
increasing the input current or decreasing the discharge zone dimension
along the flow direction will improve the light intensity in the cavity and
the output power.

2. Effects of mirror length and position

In order to test the effects of the mirror length, we computed the light
intensity at the center of the mirror and the output power for a 3 cm high
mirror with its leading edge at x = 1 cm and a length of 3, 5, 7, 8, 9, 10, 12,
14, and 17 cm. The output power is

$$W = \bar{I} \cdot A \cdot C$$

where $\bar{I}$ is the average light intensity along z, A is the area of the mirror
and C is the output coupling coefficient (taken to be 0.28). Figure 3 shows
the variation of the output with the mirror length. The output first changes
very fast and then becomes flater. The output power is a maximum at a mirror
length of 10 cm. The power actually decreases when the mirror length is
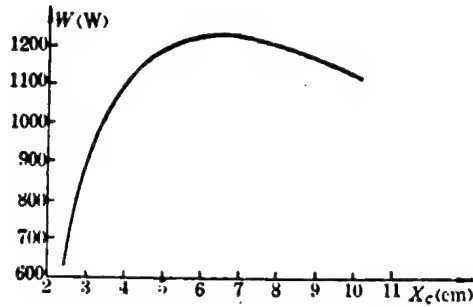increased further. The decrease in power is caused by collicion relaxation.

17

Figure 3. Output power as a function of the mirror length
(mirror center position X_c). The leading edge of
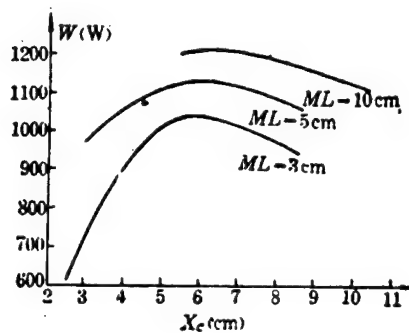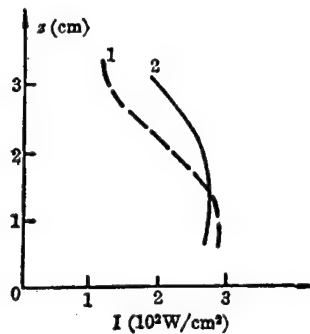the mirror is at X = 1 cm.

Figure 4. Output power as a function of the center position
of the mirror for different mirror length (ML).
For f(z) = 5 cm, G_{omax} at 5.5 cm.

Figure 4 shows the relationship between the output power and the center posi-
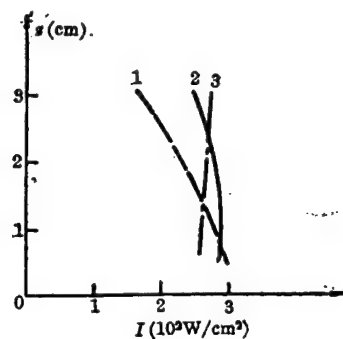tion of the mirror for fixed mirror lengths (10, 5 and 3 cm). It shows that:

(1) Regardless of the mirror length, the output power is a maximum when the
center of the mirror is placed at the peak of the small signal gain (see
Figure 7).

(2) The output power changes when the center of the mirror is moved along the
flow direction. For greater mirror lengths, the mirror covers the entire
region of the small signal gain curve (curve 2, Figure 7) and the output
variation is not large. For a shorter mirror, it covers a shorter amplifica-
tion zone and the X_c dependence of output power is greater. When the center
of the mirror is moved forward from its optimum position, the power drops
quickly. This is because the gain is small at the input of the mirror, the
discharge is insufficient and the output gain is compromised. When the mirror
is moved backward by a few millimeters, the power decreases slowly. In this
case the small signal gain at the input of the mirror is greater, the change
becomes more gradual after the peak and the vibrational energy of the dis-
charge can be derived.

18

(a) Distribution of light intensity in the z direction for a
    triangular electric field.
    Curve 1—X_c=3.5cm, I=215 W/cm²;
    Curve 2- X_c=5.5cm, I=251 W/cm²

(b) Distribution of light intensity in the z direction for a
    trapezoidal electric field.
    Curve 1—X_o=3.5cm, I=225 W/cm²;
    Curve 2—X_c=5.5cm, I=267 W/cm²;
    Curve 3—X_c=7.5cm, I=268 W/cm²

Figure 5.   Distribution of light intensity in the z direction
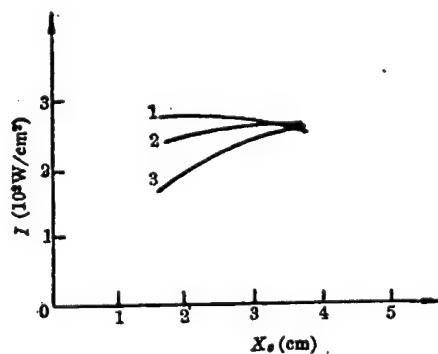

Figure 6.   Light intensity as a function of the center position
            of the mirror for different electrode width
            Curve 1--f(z) = 3.8 cm;
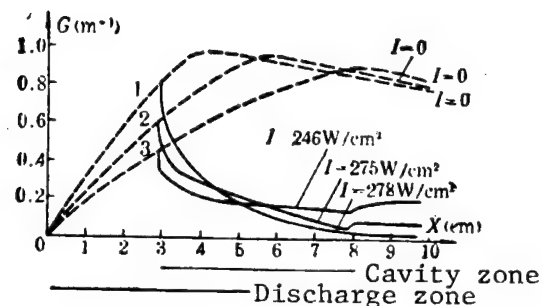   Curve 2--f(z) = 5.5 cm;
            Curve 3--f(z) = 8 cm

19

Figure 7. Small signal gain and saturation gain at different height

Curve 1--f(z) = 3.8 cm;

Curve 2--f(z) = 5.5 cm;

Curve 3--f(z) = 8 cm

(3) The output powers of a 5 cm mirror and a 3 cm mirror placed at the optimum position are lower than that of the 10 cm mirror by 9 percent and 14 percent respectively. This shows that the cavity loss using a small mirror is greater but not too great.

We now investigate the effects on the z direction distribution of the intensity and the output power by the position of a given (3x5 cm^2) mirror. For a fixed cavity position, Equation (2) indicates that the discharge zone is narrow for small values of z. For the same total current J, the electron density should be greater and the small signal gain can reach its maximum more quickly (curve 1, Figure 7). If we then place the leading edge of the mirror at the peak of the small signal gain, then the light intensity and the output power will be greater for a smaller value of z. When z is large, the discharge zone becomes longer, the electron density decreases correspondingly and the peak of the small signal gain moves backward (curves 2 and 3 in Figure 7). If the position of the mirror is fixed, the gain is smaller at a greater z in the cavity and less light intensity can be derived. This causes the light intensity I (or output power) to drop as z increases and explains the z dependence of the curves in Figure 5. Such distribution depends strongly on the shape of the electrode and the position of the cavity.

Actual measurements showed, however, that the peak position of the small signal gain was not very sensitive to changes in z. This is because that electron densities at various heights were treated as homogeneous distributions in the discharge model in this work. Moreover, the discharge zone changes substantially with height in this model and hence exaggerating the z dependence. Corrections will be made in future modifications of the model. The calculation did explain the effects of n_e on G_o and I and the criterion for the optimum cavity position based on the peak position of the small signal gain is essentially consistent with the experiments.

For given initial conditions, the z distribution of the light intensity on the mirror surface and the output power depend on the position of the mirror. Figure 5(b) shows the z dependence of the light intensity with the center of the mirror X_c at 3.5, 5.5, and 7.5 cm. As X_c moves backward, the z distribution

of the intensity becomes more uniform because all the usable gains at different heights in the entire cavity are near their peak values. Figure 6 shows the relationship between the light intensity (output power) and mirror position for different electrode widths. Each curve has its own optimum mirror position and the maximum light intensities (output power) of the curves do not vary greatly. The optimum position moves back as $f(z)$ is increased. This can also be explained by the distribution of the small signal gain and the different efficiency in the cavity. These dependences show that the output power not only depends on the electron density and width of the discharge zone but also on the relative position of the mirror and the electrode. For electrodes of the needle-plate or tube-plate structure, the effective usage of the gain is different at different z levels since the width of the discharge depends on z. The initial position of the mirror should be such that gains at various z levels in the cavity are effectively utilized.

3. Relationship between flow speed and mirror position

Because the gain curve is affected by the flow speed,[1] so is the optimum mirror position. For a flow speed of $u = 70$ m/s, the light intensity is more uniform and the output power is higher when the mirror center is at $X_c = 7.5$ cm. However, the optimum position is between $X_c = 3.5$ and 5.5 cm for $u = 30$ m/s (see Figure 8 and Table 1). The results depend sensitively on the gain distribution. For the operating conditions considered here, $X_c = 4$ cm for $u = 30$ m/s and $X_c = 7.5$ cm for $u = 70$ m/s.
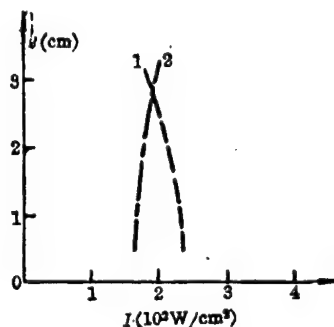

Figure 8. Relationship between mirror position and light
intensity for a flow speed of 30 m/s
Curve 1--$X_c = 3.5$ cm, $\bar{I} = 198$ W/cm^2 (trapezoidal field)
Curve 2--$X_c = 7.5$ cm, $\bar{I} = 169$ W/cm^2

Table 1. Relationship Between Light Intensity, Output Power, and Mirror
Position. (X_c is the mirror center position and the mirror
length is 5 cm)

u	30 m/s			70 m/s		
X_c(cm)	3.5	5.5	7.5	3.5	5.5	7.5
$\bar{I}$(W/cm^2)	198	197.7	169	225	267	268
W(W)	832	830	710	945	1121	1126

4. Effects of output coupling coefficient

For given discharge zone profile, mirror position and operating conditions, the output power depends on the output coupling coefficient. The coupling corresponding to the maximum power is called the optimum coupling. The optimum coupling depends on the mirror position.

Figure 9 shows the output power as a function of the coupling coefficient for a trapezoidal discharge zone (anode width = 8 cm, cathode width = 3 cm) and a mirror 5 cm long and 3 cm tall. The average light intensity is based on the intensity at the half height of the cavity. Curves 1 and 2 correspond respectively to X_c = 5.5 cm and 3.5 cm. As can be seen, the cutoff coupling is greater for curve 1 and both curves have an optimum coupling between 15 and 21 percent. It can also be seen that the output power drops rapidly when the coupling is less than the optimum but drops slower when the coupling is greater than the optimum. The discharge model[2] used in this work is still rather crude and the computed optimum coupling does not agree accurately with the measured value. The optimum coupling is best determined experimentally in the vicinity slightly greater than the computed optimum coupling. Experimental results on JL6A showed that the intensity is greatest and changed the least when the coupling was 20-30 percent, in agreement with the above conclusion.
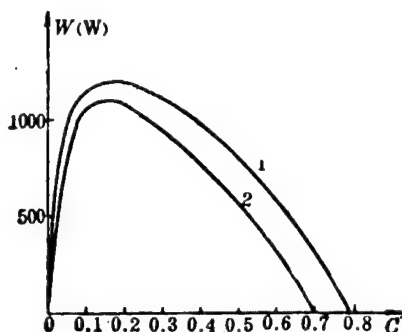

Figure 9. Relationship between output power and coupling in a trapezoidal electric field
Curve 1--X_c = 5.5 cm; Curve 2--X_c = 3.5 cm

Figure 10 shows the results for plate electrodes (triangular discharge zone). The results are similar to that in Figure 9 except that the decrease in power is even more rapid when the coupling is less than the optimum value and the change in output power is even more gradual when the coupling is greater than the optimum value.

Figure 11 shows the relationship between the output power and the coupling for different electrode widths (corresponding to different z). The figure shows that, for different electrode widths, the optimum and cutoff coupling are different. Under the given conditions, the cutoff coupling has a maximum variation of about 10 percent and the optimum coupling has a maximum variation of about 5 percent. Such variation can also be explained in terms of the differences in electron density.
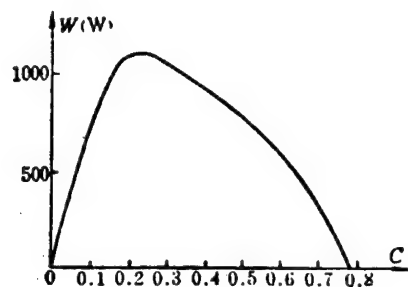
Figure 10. Relationship between output power and coupling in a triangular electric field
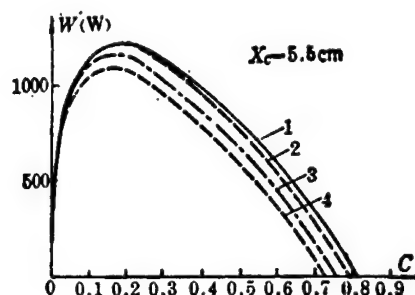$X_c = 5.5$ cm

Figure 11. Output power as a function of the coupling for different electrode widths
Curve 1--f(z) = 3.8 cm; Curve 2--f(z) = 5.5 cm;
Curve 3--f(z) = 7.2 cm; Curve 4--f(z) = 8 cm

When the electrode distance changes, E/N changes correspondingly. Figure 12 shows the effect of E/N on the coupling. When E/N is in the $2.8-2.0 \times 10^{-16}$ V·cm range, the output power and the cutoff coupling increase with E/N, but the optimum coupling does not change very much, only about 6 percent. The effect of E/N on the optimum coupling is therefore not large.
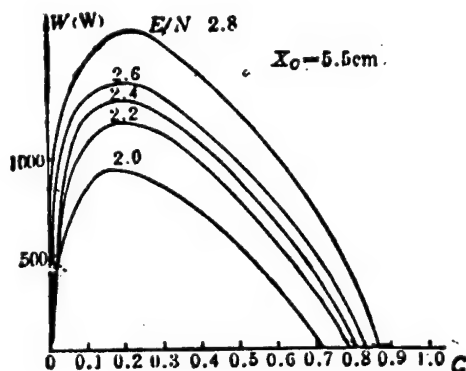

Figure 12. Output power versus coupling for different E/N
$E/N = (2.0 \sim 2.8) \times 10^{-16}$ V·cm²;
$f(z) = 5.5$ cm

23

REFERENCES

1. Chen Liyin, et al., GUANGXUE XUEBAO [ACTA OPTICA SINICA] Vol 5, No 2,
    pp 135-142, 1985.

2. Chen Liyin, et al., ZHONGGUO JIGUANG [CHINESE JOURNAL OF LASERS] Vol 11,
    No 5, pp 257-262, 1984.

APPLIED SCIENCES

UV NITROGEN LASER USING HYDROGEN THYRATRON AS SWITCH

[Article by Ou Zhenya [2962 7201 0088] and Yang Liming [2799 4539 2494] of
Qinghua University and Song Zhanxia [1345 0594 0204] of the National Standard
Bureau]

[Text] Abstract: A UV nitrogen laser, which uses a domestic hydrogen
thyratron as a switch and an isotope as a preionizer, is reported. The
maximum pulse energy is 5 mJ, the time delay jitter is ±1 ns, and the energy
stability for a single laser pulse is 5 percent.

All the nitrogen lasers made in China today have spark triggers. Spark
triggers have a simple structure and are easy and inexpensive to produce,
but they also have some problems. Problems such as unstable triggering and,
sometimes, extra or missed triggers cause large drifts in the pulsed laser
energy, especially at low repetition rates. Jitters in the pulse delay make
the synchronization very difficult, and the spark trigger is more susceptive
to electromagnetic interference. The above difficulties can be overcome when
a hydrogen thyratron is used as a trigger.

Reports[1] on triggering nitrogen lasers with a hydrogen thyratron began to
appear abroad since 1973. Some quality products began to appear in 1977.
We have made an experimental study of the hydrogen thyratron as a trigger,
with energy storage and transfer by ceramic capacitors, preionization by an
isotope, and shielding by the metallic outer case. An equivalent circuit was
proposed for calculating the circuit parameters.

I. Circuit Principle

We used a capacitive transfer circuit, shown in Figure 1. The electrooptic
characteristics of the laser cavity can be found in Ref. 2 and are omitted
from here. We shall only analyze the energy transfer efficiency in charging
C_2 by C_1 and the effects of the peak current and capacitance ratio of the
thyratron. In the process, there was no breakdown emission in the laser
cavity. Calculation[2] showed a low electrical conductivity. It can there-
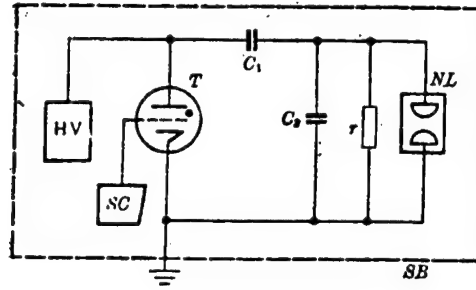fore be viewed as an open circuit without affecting the results below.

Figure 1. Circuit diagram of the nitrogen laser

HV--DC high voltage source 0.25kV
 r--1 kΩ resistance
 T--Ceramic hydrogen thyratron
NL--Laser cavity, electrode length = 800 mm, discharge
    area = 10x25 mm
C_1--Storage capacitor (ceramic), 30 nF
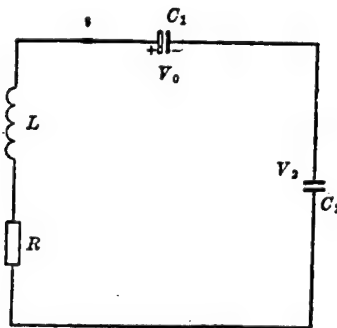C_2--Transfer capacitor (ceramic), 22 nF
SB--Shielding box

Figure 2. Equivalent circuit for energy transfer between the
          capacitors

The circuit equation is

$$L\frac{di}{dt} + Ri + \frac{1}{C_2}\int_0^t i\,dt = V_0 - \frac{1}{C_1}\int_0^t i\,dt \tag{1}$$

and the solution is

$$i = \frac{C\omega_0^2}{\omega} V_0 e^{-\frac{t}{\tau}} \sin \omega t \tag{2}$$

$$V_2 = \frac{C\omega_0}{C_2\omega} V_0 \left[\frac{\omega}{\omega_0} - e^{-\frac{t}{\tau}} \cos(\omega t - \theta) \right] \tag{3}$$

where

$$C = \frac{C_1 C_2}{C_1 + C_2}, \quad \omega_0^2 = \frac{1}{LC}, \quad \tau = \frac{2L}{R},$$

$$\theta = \sin^{-1} \frac{1}{\omega_0 \tau}, \quad \omega^2 = \omega_0^2 - \frac{1}{\tau^2}.$$

Since the value of R used is very small and $0 < t \leqslant \frac{\pi}{\omega}$, the following conditions are satisfied:

$$\omega_0 \gg \frac{1}{\tau}, \quad \omega \approx \omega_0, \quad t/\tau \approx 0 \quad \text{and} \quad \theta \approx 0.$$

The two equations above can therefore be simplified to

$$i = C \omega_0 V_0 \sin \omega_0 t \qquad \qquad (4)$$

$$V_2 = \frac{C}{C_2} V_0 (1 - \cos \omega_0 t) \qquad \qquad (5)$$

(1) Energy transfer efficiency η for C_1 to C_2 charging

The energy of the laser pulse depends mainly on the energy stored in C_2. Based on (5), the energy in C_2 is a maximum when $t = \pi/\omega_0$. The maximum laser intensity will be obtained by adjusting the nitrogen pressure and inducing a discharge at this time.

$$\eta = \frac{1}{2} C_2 V_{2\,\text{max}}^2 \bigg/ \left(\frac{1}{2} C_1 V_0^2 \right) = \frac{4n}{(1+n)^2}$$

where $n = C_2/C_1$. When $n = 1$, η is 100 percent. At $n = 0.7$, η is 97 percent.

(2) Peak current i_{max} of the thyratron

From (4), the maximum current occurs at $t = \pi/2\omega_0$ and is equal to

$$i_{\text{max}} = \left[\frac{nC_1}{(1+n)L} \right]^{\frac{1}{2}} V_0$$

When n changes from 1 toward zero, i_{max} decreases. A small value of n is good for the thyratron but not for the energy transfer. After weighing the advantages and disadvantages, we chose n = 0.7. The value of L is known to be 0.5 µH. We also selected C_1 = 0.03 µF, V_0 = 20 kV, and obtained i_{max} = 3 kA.

Hydrogen thyratrons made in China meet the above requirement and can handle an anode peak current of 20-30 kA and a cathode voltage higher than 20 kV.

It should be noted that, from economic and other considerations, it is permissible to operate above the peak value. However, cautions should be used in exceeding the peak current as it shortens the service life of the thyratron and is also not economical.

27

II. Experimental Results

All the components are installed in a metal shield to prevent external electromagnetic interferences. In the gas system, an isotope preionizer is installed to improve the stability of the laser pulses. Measurements are made using a RK-3230 (336 probe) thermoelectric energy meter. Using single-shot manual triggering, we measured the laser pulse energy for 50 consecutive pulses and the results are shown in Figure 3, where the solid line is the average energy of 5.56 mJ. Points between the two dashed curves have an energy fluctuation value less than or equal to ±5 percent of the average value. Only three data points had a greater fluctuation. We can therefore claim that the stability (90 percent pulse number) is ±5 percent, it is the best stability[3] achieved for the nitrogen laser here and abroad.
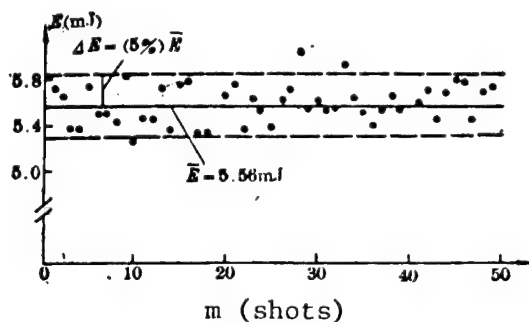

m (shots)

Figure 3. Distribution of the laser pulse energy

Using a photodiode as a receiver, the integrated pulse was displayed on an oscilloscope. The peak value is proportional to the laser pulse energy (see Figure 4). For repetition rates below 10 Hz, the energy is unaffected. At higher repetition rates, the energy decreases. The decrease is 10 percent at 20 Hz.
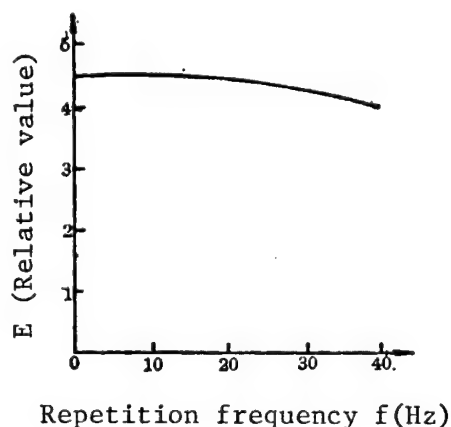

Repetition frequency f(Hz)

Figure 4. Laser energy E as a function of repetition frequency f

The pulse widths of the nitrogen laser and the pumping dye laser are only a few nanoseconds. When several lasers are used, synchronization is needed so that the delay jitters are no more than 1 or 2 ns.

We measured the delay jitters of a small nitrogen laser with low C_1, C_2, and rated peak current of the hydrogen thyratron.

Using a TF1850 tube as the receiver, the steep edge may reach 1 ns. The response frequency of a SS-5321 S oscilloscope used in the laser waveform observation can reach 250 MHz. Figure 5(a) shows a laser waveform obtained using the internal trigger of the oscilloscope, the waveform line is thin. Figure 5(b) shows the same waveform obtained with the synchronous external trigger and the trace line becomes thick due to the delay jitters of the hydrogen thyratron (including the laser cavity). Taking the half-width of the trace as the delay jitter $\Delta\tau$ of the laser, we have

$$\Delta\tau = \pm 1 \text{ ns}$$

This shows that the Chinese made nitrogen laser triggered by a hydrogen thyratron has a small delay jitter and can be synchronized.
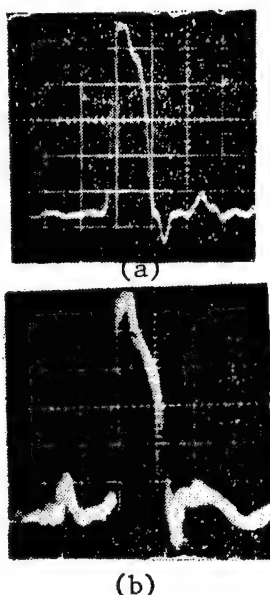

Figure 5. Laser waveform

Horizontal axis: time (10 ns/div), Vertical axis: intensity (relative)
(a) Triggered by internal trigger of oscilloscope
(b) Triggered externally

It should be pointed out that a number of factors contribute to the delay jitter. Examples are the steepness and height of the thyratron trigger voltage, filament voltage stability, quality of the thyratron, and internal pressure of the laser cavity. Careful adjustments and selections must be made in the experiments.

29

When the nitrogen laser discharges, it produces strong electromagnetic interference in the vicinity, affecting the normal function of electronic instruments and leading to large measurement discrepancies. The interference is greatly reduced when all the components are enclosed in a small case. Using a thyratron in place of the spark trigger, the interference is a minimum.

We have described some of the advantages of the hydrogen thyratron, but the price of a thyratron is high and the economic payoff depends directly on the life of the thyratron. We have developed a total of five such lasers and all the thyratrons have functioned normally. One of the units has been in use for 3 years and another unit, with microprocessor controlled data acquisition and processing, has been used in uranium acyl ion laser induced fluorescence spectral measurements with good economic payoff.

REFERENCES

1. Woodward, B.W., et al., Rev. Sci. Instrum., 1973, 44, 882.

2. Fitzimmons, W.A., et al., IEEE J. Quant. Elect., 1976, QE-12, No 10, 624.

3. Molectron UV Series II Nitrogen Lasers, Molectron Corporation, California, 1980, 1-4.

9698/6091
CSO: 4008/79

APPLIED SCIENCES

EXPERIMENTAL STUDY OF STIMULATED RAMAN SCATTERING OF HIGH-PRESSURE H_2
FREQUENCY SHIFTER

[Article by Gao Guochang [7559 0948 2490], Li Rongping [2621 2837 1627],
Guo Ningning [6753 1380 1380], Gao Wenbin [7559 2429 2430], Chen Junde
[7115 0193 1795], and Lu Shiping [7627 1102 1627] of the Anhui Institute
of Optics and Fine Mechanics, Chinese Academy of Sciences]

[Text] Abstract: Experimental setup and results of RS-1 model high effi-
ciency high pressure H_2 Raman shifter are presented. Main factors affecting
the energy conversion efficiency are discussed. When the Raman shifter was
pumped by Nd:YAG SHG, 1st to 4th order Stokes lines and 1st to 8th anti-
Stokes lines have been observed. An overall energy conversion efficiency of
56 percent and an energy conversion efficiency of 34 percent in the 1st
Stokes component have been achieved.

I. Introduction

We have designed and developed a RS-series high pressure H_2 stimulated Raman
frequency shifters. Using sealed lens window and precision mechaning, the
energy utilization rate of the pumping beam and the frequency shift beam was
greatly improved to reach or excel the level in foreign frequency shifters
such as the Lambda Physik RS-75 Raman cell. Under 8 atm of H_2 pressure and
at an input pumping energy of 26 mJ, we have observed the first through the
eighth anti-Stokes lines. At 18 atm H_2 pressure and under the same pumping
conditions, the first through the fourth Stokes lines were observed. As com-
pared to a recent study in China,[1] the number of Stokes lines and anti-Stokes
lines and the energy conversion efficiency have shown considerable increases.

In addition, the new technology of sealed window has allowed the RS-I
frequency shifter to operate continuously under 20 atm of H_2 pressure for
18 months without any sign of leaking. The requirement of long-term safe
operation is therefore met.

II. Experimental Setup and Results

Figure 1 shows the experimental setup. The pumping laser is a Nd:YAG
frequency doubled laser with $LiNbO_3$ crystal Q-switching. The output

wavelength is 532 nm and the pulse width is 15 ns. The 1.06 µm total reflection plate eliminates the residual 1.06 µm light after frequency doubling. The RS-I Raman frequency shifter is made of a stainless steel body and the lens window is sealed. The stainless steel body houses the inner H_2 cell, the outer liquid N_2 jacket, the high pressure control valve and the H_2 pressure monitor. A pair of confocal lenses serves the function of pressure seals and focusing. Pinhole caps are installed outside the lens window for alignment and serve as dust covers.
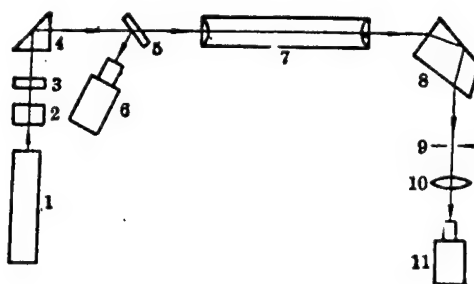

Figure 1. Experimental setup

1--Nd:YAG laser; 2--KDP frequency doubling crystal; 3--1.06 µm total reflection plate; 4--Right-angle total reflection prism; 5--Beam splitter; 6, 11--Laser energy meters; 7--RS-I frequency shifter; 8--Pellin-Broca prism; 9--Variable aperture diaphragm; 10--Focusing lens

The Pellin-Broca prism is used for beam splitting and for deflecting the output beam by 90°. The energy meter is a calibrated NJ-J1 laser energy meter. By rotating the Pellin-Broca prism fixed on a model QJG grating platform, the various order Raman beam and the residual pumping beam consecutively pass through diaphragm 9 and lens 10 accurately enter the energy meter 11. The purity of the hydrogen gas is 99.99 percent and the entire experiment is conducted at an ambient temperature of 18°C.

At a pumping laser energy of 26 mJ and a hydrogen pressure in the frequency shifter ranging from 20-2 atm, the energies of the first order Stokes line (S_1) and the first through the third anti-Stokes lines (AS_1-AS_3) are shown respectively in Figures 2 and 3.

When the H_2 pressure is 13 atm, the output energies of S_1 and AS_1 measured by changing the incident pumping light energy are shown in Figure 4 as functions of the pumping energy.

For a pump energy of 26 mJ and a H_2 pressure of 8 atm, the measured output energies of S_1 and AS_1-AS_7 are compared with the pump energy in Figure 5.

At a pump energy of 26 mJ and a H_2 pressure of 20-2 atm, the order of the anti-Stokes frequency shift is observed on the fluorescent paper screen. The distribution is shown in Table 1.
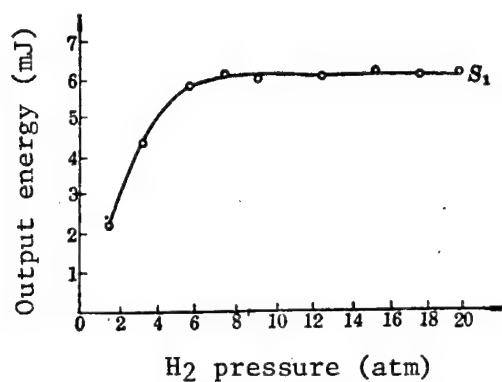
Figure 2. S_1 output energy versus H_2 pressure.
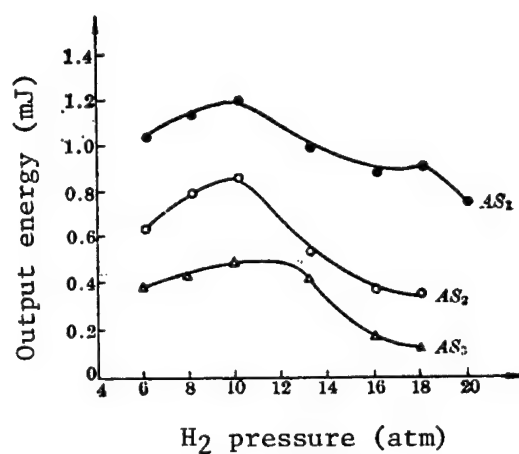(Pumping laser has an energy of 26 mJ)

Figure 3. Output energies of AS_1, AS_2, and AS_3 versus H_2 pressure.
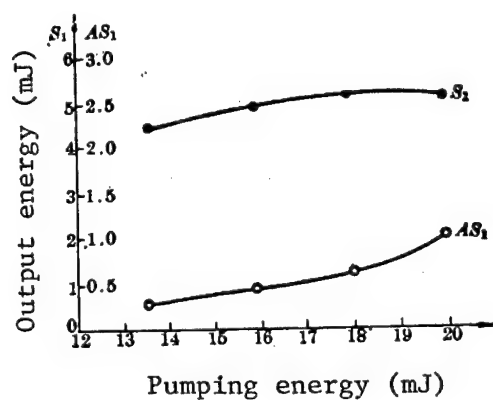(Pumping laser energy = 26 mJ)

Figure 4. S_1 and AS_1 output energies versus the pumping energy.
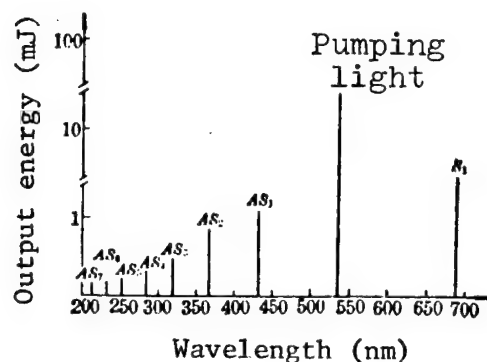(H_2 pressure = 13 atm)

Figure 5. Output energies of S_1 and AS_1–AS_7 as compared to the pump energy. (H_2 pressure = 8 atm, pump energy = 26 mJ)

Table 1. Order of the Anti-Stokes Frequency Shift Observed Under Different H_2 Pressure

H_2 pressure (atm)	20	18~13	8~6	4	2
Orders of the light spots	AS_1 ~AS_3	AS_1 ~AS_5	AS_1 ~AS_8	AS_1 ~AS_7	AS_1 ~AS_6

In the visible and ultraviolet region, the wavelengths of the various order frequency shifted light are measured with a model AAS_1 atomic absorption spectrophotometer and a model AC 15/5 complex projection galvanometer. The accuracy of the AAS_1 is ±0.1 nm. The H_2 pressure is 8 atm and the pump energy is 26 mJ during the measurements. The results are shown in Table 2.

Table 2. Detected Wavelengths at 8 atm H_2 Pressure

Order of the frequency shifted light	S_1	AS_1	AS_2	AS_3	AS_4	AS_5	AS_6	AS_7	AS_8
Center wavelength (nm)	683	435.7	368.9	319.8	282.3	252.7	228.6	208.8	192.1

For higher orders of Stokes lines, their energies were not measured because the spot position could not be accurately determined due to the lack of an upper conversion material. For the S_4 line, we used a model TGS infrared camera and monitor with a Ge window. The camera tube was equipped with a Ge lens, the short wavelength limit was 1.8 μm, and the S_3 (with a wavelength of 1.579 μm) could not pass through. After the camera captured the light spot by rotating the Pellin–Broca prism, the camera was moved back and forth and no noticeable spot size changes were observed, indicating that the spot was coming from a laser. We believe it is a S_4(λ = 4.59 μm) spot. Moreover, we measured the infrared transmissivity of the quartz material in the optical path; a small transmission was observed at 4.5 μm. It was therefore possible to have some transmission at a high light intensity, which lent further support to our assessment.

34

III. Discussion

The energy conversion efficiency is an important technical parameter of a frequency shifter. The energy conversion efficiency is defined as the energy ratio of the frequency shifted light to the imput pump light. Our tests show that the conversion efficiency is affected by the following factors:

1. Quality of the shifter

Commonly used shifters may be divided according to their construction into type A that requires an external focusing lens and type B with a lens window. Under the same conditions a type A suffers about 20 percent more light energy loss than a type B shifter and costs about 30 percent more to operate. The RS-I shifter is a type B shifter and it has good transmissivity and efficiency.

2. Purity of the H_2 gas

The conversion efficiency was low in earlier experiments because of insufficient outgassing. The efficiency has been substantially improved by increasing the purity of the H_2 gas in the gas cell.

3. Pump energy and H_2 pressure

The relationships between the conversion efficiency and the pump energy and the H_2 pressure are very complex. The pump energy and the gas pressure must be determined based on the desired output wavelength.

4. Length of the shifter

Generally speaking a longer shifter has a lower threshold for the same H_2 pressure and pump conditions. A longer shifter in general has a higher efficiency but there is a limit to the length.

5. Sealing of the shifter

How good a shifter is sealed not only affects the safety of the operation but also the conversion efficiency. The RS-I shifter employs a new sealing technique and has been continuously operated for 18 months at 20 atm H_2 pressure without leaking.

6. Temperature

The conversion efficiency is improved by using low temperature cooling gas. It was reported in Ref. 2 that the use of liquid nitrogen coolant improved the AS_7 energy by a factor of 2. Our experiment results on liquid nitrogen cooling will be reported elsewhere.

[2799 4539 2579], Dong Chenggong [5516 2052 0501], Li Guangmao [2621 0342 5399], Zhan Heying [6124 0678 5391], Cao Xiaowen [2580 2400 2429], Hu Xiangkui [5170 6272 7608], Chen Wenzhuo [7115 2429 3820], and Qian Jun [6929 6511].

REFERENCES

1. Guo Yili, et al., WULI XUEBAO [ACTA PHYSICA SINICA] Vol 34, No 1, p 24, 1985.

2. D.J. Brink and D. Proch, Laser and Optoelektronik, No 3, pp 41-48, 1982.

DISORDER AND LOCALIZATION OF ELECTRONIC STATES IN METALLIC SUPERLATTICES

[English abstract of article by Xiong Shijie [3574 6108 2638]; paper received 14 May 1984]

[Text] The position of the mobility edges in disordered metallic super-lattices has been calculated by studying the electronic states for a simplified Hamiltonian model using Anderson's localization theory.

REFERENCES

[1] T.Jarlborg and A.J. Freeman, Phys. Rev. Lett. **45** (1980) 653.

[2] 熊诗杰，蔡建华，物理学报，**31** (1982) 474.

[8] P.W.Anderson, Phys.Rev. **109** (1958) 1492.

[4] J.M.Ziman, J.Phys. C**2** (1969) 1230.

/6091
CSO: 4009/1116

RESEARCH ON OPTIMUM DESIGN OF MACHINE TOOL STRUCTURES

[English abstract of article by Tan Li [6223 0500], Ge Qiaoqin [5514 1564 3830], Wen Wenyuan [3306 2429 3293], and Pan Xinlu [3382 2450 7120] of the Department of Mechanical Engineering; paper received 11 November 1984]

[Text] An approach to combine the mathematical programming method with mechanical approximation to optimize the machine tool structures is presented in this paper. In our case, the problem of structure optimization is converted into a nonlinear programming problem with dynamic and static characteristical constrains.

An approximation technic is employed to generate a sequence of mathematical programming for sub-problems with explicit constrains which is easy to solve.

Therefore, the amount of computation work for structure analysis by finite element method is reduced greatly.

The usefulness of this procedure is shown from the optimized results of several structure models and realistic lathe beds.

REFERENCES

[1] 钱令希：《工程结构优化设计》，水利电力出版社，1983年。

[2] Fleury. C. and Schmit. L. A.: ACCESS3. Approximation concepts codes for efficient structural synthesis user's guide, NACA CR-195260, 1980.

[3] 温文源、葛巧琴、虞尔九、潘新陆：机床结构件振动特性的有限元法计算研究，第二届机床设计与研究年会论文集，1980年。

[4] James A. Bennett and Mark F. Nelson: An optimization capability for automative structures, SAE, 1980, 3236—3244。

[5] 谭 力，葛巧琴，温文源，潘新陆：机床结构件优化设计的初步研究，第三届机床设计与研究年会论文集，1984年。

LARGE-CORE DOUBLY CLAD SINGLE-MODE OPTICAL FIBERS

[English abstract of article by Jiang Shijun [5592 2514 6511] and Lin Zhiyuan [2621 1807 3850] of the Department of Electronic Engineering; paper received 13 October 1984]

[Text] This paper presents the propagation characteristics of double clad single-mode fibers having core with α power index distribution and discusses the effect of the central dip in the refractive index caused in MCVD method. According to the theoretical calculations we have first fabricated some large-core doubly clad single-mode fibers. Their diameters reach 14-17 μm which are about two times that of the conventional single clad single-mode fiber. In addition, their bending loss is very small.

REFERENCES

[1] Unger, H. G.: Planar Optical Waveguides and Fibers, Clarendon, Oxford, 1977, 467.

[2] Gambling, W. A. et al.: Propagation in radially inhomogeneous single-mode fibre, Opt. Quant. Elect., Vol. 10, 1978, 31.

[3] Cohen L. G. et al.: Tailoring the shapes of dispersion spectra to control bandwidths in single-mode fibers, Opt. Lett., Vol. 7, 1982, 183.

[4] 盛嘉茂：用高斯近似计算单模 α 光纤的色散参数，《光通信研究》1982年，第 4 期。

[5] Andreer, A. T. et al.: Experimental study of single-mode W-type optical fiber, Elect. Lett., Vol. 17, 1981, 416.

THE PREPARATION AND CRYSTAL STRUCTURE OF TRINUCLEAR MOLYBDENUM CLUSTER COMPOUND $(Me_4N)[Mo_3(\mu_3-O)(\mu-Cl)_3(\mu-O_2CH)_3Cl_3]$

[English abstract of article by Lin Xianti [2651 6343 2748], Huang Jinling [7806 6855 7117] of Fujian Institute of Research on the Structure of Matter, Chinese Academy of Sciences, Fuzhou, and Huang Jianquan [7806 1696 0356] of the Department of Chemistry, Fuzhou University, Fuzhou; paper received 22 May 1984]

[Text]   The title compound was prepared through oxidation of $MoCl_3$ in the liquid phase. The crystal belongs to the orthohombic system with space group D_{2h}^{16}-Pmnb and unit cell parameters: a = 11.403(1), b = 12.345(2), c = 14.292(2)Å, V = 2011.8(8)Å^3; Z = 4, D_c 2.396 g/cm^3. The 2303 independent reflections were collected on a CAD4 four-circle diffractometer with Mo Kα radiation in a range $2 \leqslant \theta \leqslant 27$. The crystal structure was solved by heavy-atoms method and refined by a full matrix least-squares technique to final discrepancy factors R = 0.050 and R_w = 0.056 for 1513 reflections of $I \geqslant 3\sigma(I)$. The configuration of cluster anion was characterized to have the same M1 type structure as presented in a previous paper. The average bond lengths Mo--Mo is 2.577Å, Mo--O-μ_3 is 1.982Å. In addition, relation of Mo--Mo bonds with the bridging atom, bond order, and other lignds coordinated to the Mo atom is discussed briefly.

REFERENCES

[1] 林贤梯, 黄金陵, 黄建全, 科学通报, **1984**, *29*, 1216.

[2] 黄金陵, 商茂虞, 黄建全, 有机化学, **1983**, 326.

[3] (a) Cotton, F. A., *Inorg. Chem.*, **1964**, *3*, 1217; (b) Müller, A.; Jostes, R.; Contton. F. A., *Angew. Chem., Int. Ed. Engl.*, **1980**, *19*, 875.

[4] (a) Scavnicar, S.; Brown, C. J., *Acta Cryst.*, **1966**, *21*, 151; (b) Herceg, H.; Scarnicar, S., *Croat. Chem.Acta*, **1967**, *39*, 187; (c) Grdonic, D.; korpar-Colig, B., *Proc. Chem. Soc.*, **1963**, 308

[5] Bino, A.; Cotton, F. A.; Dori, Z., *J. Am. Chem. Soc.*, **1978**, *100*,. 5252.

[6] Bino, A·; Cotton, F. A.; Dori, Z., *J. Am. Chem. Soc.*, **1979**, *101*, 3842.

[7] Müller, A.; Ruck, A.; Darttmann, M.; Rcinsch-Vogell, U., *Angew. Chem. Int. Ed. Engl.*, **1981**, *20*, 483.

[8] (a) McCarroll, W. H.; Katz, L.; Ward, R., *J. Am. Chem. Soc.*, **1957**, *79*, 5410; (b) Ansell, G. B., Katz, L., *Acta Cryst.*, **1966**, *21*, 482.

[9] Bino, A.; Cotton, F. A.; Dori, Z., *Inorg. Chem. Acta*, **1979**, *33*, L133.

[10] 吴鼎铭, 庄鸿辉, 郑建基, 黄金陵, 卢嘉锡, 黄建全, 中国科学, *B* 辑, 待发表.

[11] Wu. D. -M.; Zhuong, H. -H.; Zheng, J-J.; Huang J. -L; Lu, J. -X.; Huang, J. -Q., *J. Struct. Chem.* **1984**, *3*, 51.

[12] 商茂虞, 黄金陵, 卢嘉锡, 中国科学, *B* 辑, **1984**, 875.

[13] 吴鼎铭, 庄鸿辉, 郑建基, 黄金陵, 卢嘉锡, 黄建全, 中国科学, *B* 辑, 待发表.

[14] 吴鼎铭, 黄金陵, 黄建全, 待发表.

[15] 卢绍芳, 商茂虞, 黄金陵, 黄建全, 中国科学, 待发表.

[16] 庄鸿辉, 黄金陵, 黄建全, 郑建基, 待发表.

[17] 林贤梯, 林玉辉, 黄金陵, 黄建全, 科学通报, 待发表.

[18] 卢绍芳, 黄金陵, 黄建全, 中国科学, 待发表.

[19] Müller, A.; Reinsch-Vogell, U., *Angew.Chem.*, *Int. Ed. Engl.*, **1980**, *19*, 72.

[20] Vergamini, P. J.; Vahrenkamp, H.; Dalrl, L. F., *J. Am.Chem. Soc.*, **1971**, *93*, 6327.
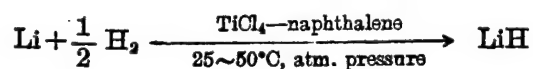
CATALYTIC SYNTHESIS OF LITHIUM HYDRIDE UNDER MILD CONDITIONS

[English abstract of article by Liao Shijian [1675 0013 0256], Kong Wei [1313 1550], Liu Hezhong [0491 0735 5883], Li Jingkui [2621 4737 1145], and Xu Yun [1776 4596] of the Dalian Institute of Chemical Physics, Chinese Academy of Sciences, Dalian; paper received 28 June 1984]

[Text] A method for the catalytic synthesis of lithium hydride under mild conditions is presented. The catalyst is composed of titanium tetrachloride and naphthalene or its methyl derivatives and has a very high activity.

$$Li + \frac{1}{2} H_2 \xrightarrow[\text{25$\sim$50°C, atm. pressure}]{\text{TiCl}_4\text{—naphthalene}} LiH$$

Metallic lithium can be quantitatively hydrogenated to lithium hydride at 25-50°C under atmospheric pressure within 2-5 h according to various catalyst compositions. The catalyst stability has been investigated and the relationship between catalyst compositions and reaction controlling step has been established also.

REFERENCES

[1] Sullivan, E. A.; Wade, R. C., *"Kirk-Othmer Encyclopedia of Chemical Technology"*, Vol. 12, 3rd Ed, 1980, p. 772.

[2] Bogdanovic, B.; Liao, S. T.; Schwickardi, M.; Sikorsky, P.; Spliethoff, B., *Angew. Chem.*, 1980, *92*, 845; idem, *Angew. Chem.*, *Int. Ed. Engl.*, 1980, *19*, 818.

[3] Bogdanović, B.; Liao, S. T.; Schlichte, K., *"Abstr. of the 3rd. Int. Symp. on Homogeneous Catalysis"*, Milano-Italy, 1982, p. 104.

[4] 刘和众, 廖世健, 化学通报, 1984, *4*, 27.

[5] 廖世健, 徐筠, 刘和众, 化学通报, 1983, *(12)*, 25.

[6] Martin, H.; Stedefeder, J., *Justus Liebigs Ann. Chem.*, 1958, *618*, 17.

/6091
CSO: 4009/1118

RESEARCH ON COLOR REACTION BETWEEN BISMUTH(III) AND THIAZOLYLAZO-DERIVATIVE

[English abstract of article by Gao Jialong [7559 1367 1727], Bai Hao [4101
4110] of the Institute of Urban Construction and Environmental Protection,
Suzhou, Wang Xiaoming [3769 2556 2494], and Chen Tongyue [7115 0681 1471] of
the Department of Chemistry, Lanzhou University, Lanzhou; paper received
19 April 1983, finalized 28 December 1984]

[Text] A new chromogenic reagent, 2-(4,5-dimethylthiazolylazo)-5-diethyl
aminophenol, DMTAE, has been synthesized by coupling of 2-amino-4,
5-dimethylthiazole with m-dialkylaminophenol. The blue complex formed
between Bi(III) and DMTAE at pH 2.8 (potassium biphthalate buffer solution)
has been investigated. Molar absorptivity is $1.0 \times 10^5 \mathrm{L \cdot mol^{-1} \cdot cm^{-1}}$ at λ_{max}
590 nm. The analytical specificity is $K_{a1} = 7.6 \times 10^{-2}$, $K_{a2} = 1.0 \times 10^{-7}$. The
composition of complex as determination by a variety of methods is Bi(III):
DMTAE (1:2). The apparent stability constant calculated is 2.9×10^9. A
highly sensitive method for spectrophotometric determination of microquantity
of bismuth has been developed, which is suitable for the determination of
microamounts of bismuth in tool steel, bronze, copper alloy, waste water
and tap water.

REFERENCES

[1] Sproull, R. C.; Getter, A. O., *Ind. Eng. Chem. Anal. Ed.*,**1941** *13*, 462; Nielsch, W.; Böltz, G.,*Z.Anal. Chem.*, **1954**, *142*, 321.

[2] Yamane, T.; Suzuki, T.; Mukoyama, T., *Anal. Chim. Acta*, **1972**, *62*, 137.

[3] Танаев, О. А.; Шахабудинов, Щ., *Химия и Хим. Технол.*, **1973** *16*(1), 29.

[4] Шестидесятная, Н. Л.; Миляева, Н. М.; Котелянская, Л. И., *Ж. аналит. химии.*, **1975**, *30*, 522; 徐其亨，许秀君，化学学报，**1982**，*40*，419.

[5] Киш, П. П.; Балог, Й. С.; Спиваков, Б. Я.; Золотов, Ю. А., *Ж. аналит. химии.*, **1976**, *31*, 1114.

[6] Антонович, В. П.; Суворова, Е. Н.; Шелихина, Е. И., *Ж. аналит. химии.*, **1982**, *37*, 429.

[7] Саввин, С. Б.; Розовску, Ю. Г.; Прописзова, Р. Ф.; Ликонина, Е. А.; *Тамже*, **1970**, *25*, 423.

[8] 刘锡林，顾钢，陈同岳，高家隆，分析化学，**1984**，*12*，246.

[9] Inczédy, J., *"Analytical Application of Complex Equilibria"*, Wiley, New York, 1976.

[10] Smith, A. E., *Analyst*, **1975**, *100*, 300; 郭小伟，杨密云，分析化学，**1980**，*8*，466

[11] Щербов, Д. П.; Астафьева, И. Н.; Плотникова, Р. Н.; *Ж. аналит. химии.*, **1978**, *33*, 13.

A GC METHOD TO MEASURE SOME ORGANIC POLLUTANTS IN THE SEDIMENTS ON THE BOTTOM
OF THE CHEMICAL INDUSTRY WASTE WATER DRAIN

[English abstract of article by Zhao Deren [6392 1795 0088] of Changchun
College of Optics and Fine Mechanics, Long Fengshan [7893 7685 1472], and
Lang Peizhen [6745 0160 3791] of the Institute of Environmental Science of
Northeast Normal University, Changchun; paper received June 1985]

[Text] In this method, FID and ECD are used for measuring 49 organic
pollutants in the sediments on the bottom of the chemical industry waste
water drain. The retention data, response factors and calibration curves
of the 49 compounds are reported. The 49 pollutants are effectively
separated on a SP-2250 packed column with a length of 3 m.

An extraction and clean-up procedure for measuring these 49 compounds in
sediments by GC is also described. The procedure is simple, convenient and
applicable to analysis of complicated sediments which are contaminated by
chemical industry waste water.

From the sediment sample 31 organic pollutants are quantitatively measured.
And the concentration of these compounds in the sediment are as 10^2–10^4
times as in the waste water in the same drain.

Particularly, in the sediment, many organic compounds possess of toxicity
and persistency.

REFERENCES

〔1〕 樊德方主编，《农药残留量分析与检测》，上
海科学技术出版社，1982.
〔2〕 赵德仁等，第五次全国色谱学术报告公文集.
上册246页，1935年10月，成都.
〔3〕 吉林化学工业公司研究院编，《气相色谱实用
手册》，化学工业出版社，374页，1980

/6091
CSO: 4009/1122

THE SEARCHING OF X-RAY POWDER DIFFRACTION PATTERN ON MICROCOMPUTER

[English abstract of article by Chen Guanghui [5400 0342 5478], Wu Jianguo [0702 1696 0948], and Qiu Dirong [8002 4574 2837]; paper received 25 June 1984]

[Text] The searching of X-ray powder diffraction pattern on the CROMEMCO microcomputer is presented. The COBOL language is used for coding our program. About 700 JCPDS cards have been stored up for geology. We have searched some samples (including man-made samples and natural samples). We find that there are few misses and a few errors among the phases searched out. The consequences are satisfactory.

REFERENCES

[1] L. K. Frevel, Anal. Chem. 37, 471, (1965) L.K.Frevel, C.E.Adams, Anal, Chem. 40, 1335, (1968)

[2] G.G.Johnson. Jr. V. Vand, Ind, Eng. Chem, 59, 19, (1967)

[8] L.K.Frevel, Adv,.in X-ray Anal. 20, 15, (1977); Anal. Chem. 54, 691, (1982)

[4] P.F.Dismore, Adv. in X-ray Anal. 20, 113, (1977)

[5] 马礼教、许自省、王博义，应用科学学报第一卷第4期353页（1983）

[6] 林少凡、卢桂章、王祖陶、刘月亭、关栋云，南开大学学报第1期51页（1978）

[7] 林天辉、张赛珠、陈丽君、蔡新兴，J. Appl. Cryst. 16. 150，（1983）

/6091
CSO: 4009/1116

A SIMPLE ADAPTIVE BLOCK PICTURE CODING

[English abstract of article by Zhang Minli   [4545 3046 4539] and Xu Mengxia
[1776 1322 0204] of Peking University; paper received 9 February 1984]

[Text] In this paper a simple adaptive block picture coding is discussed,
which is based on block coding of (4x4) pels, and is adaptively switched to
block coding of (2x2) pels, when contours exist within the block and the
root mean square error of the processed block exceeds a given threshold
value.

Experiments with test pictures (sampling frequency 10 MHz) by computer
simulation show that, if the threshold value TH = 4, then the average bit-rate
is less than 3.2 bit/pel, the signal to noise ratio is greater than 36 dB,
and the processed pictures show no visible difference in subjective quality
when compared with the original.

REFERENCES

[1] A. Habibi, Survey of Adaptive Image Coding Techniques, IEEE Trans. Com., Vol. COM-25, No. 11,
     1977, pp. 1275~1284.
[2] 安田靖彦等, 利用分层次编码逐步由粗到细地进行图象的传输和显示, 信学志, Vol. 63-B, No. 4, 1980, pp.
     379~386.
[3] M. Kunt and O. Johnsen, Block Coding of Graphics: A Tutorial Review, PIEEE, Vol. 68, No. 7, 1980,
     pp. 770~785.
[4] 姚庆栋等编著, 图象编码基础, 人民邮电出版社, 1984 年, 第 9 章, 静态图象编码.
[5] CCIR Recommendation 500, Method for the Subjective Assesment of the Quality of Television Pictures,
     CCIR 13 th Plenary Assembly, Vol. 11, pp. 65~68, 1974.

/6091
CSO: 4009/1120

DISCUSSIONS WITH THREE SCHEMES OF ADAPTIVE DPCM INTRAFRAME PICTURE CODING

[Text]   Comparisons and discussions are made between three schemes of adaptive DPCM intraframe picture coding from Jing Donghan et al.[1], Zhang Chuntian[2,3] and the author of this paper[4]. Results of calculations (histograms, entropy values, root mean square values and peak values of prediction errors) and subjective tests (using Pirsch's 15-level quantizer) with four sets of test picture sequences (sampling frequency 10 MHz) show that: The subjective picture quality of these three schemes are similar with "Boy with Toys (Sequence)" and "RMA Test Chart (Sequence)", while the calculation results of Jing's scheme are better. With "Resolution Chart (Sequence)" and "Resolution Chart (Sequence) (mirror)", the subjective picture quality and calculation results of Zhang's scheme are better. As for hardware realization, the author's scheme is relatively simple in algorithm, and then Zhang's scheme, while Jing's scheme is relatively complex.

REFERENCES

[1] 金东瀚，安田靖彦，按邻近象素自适应的非线性预测图象编码，通信学报，第3卷(1982年)，第1期，第1～9页.

[2] Zhang Chuntian, Ein neuer Adaptiver Prediktor für die DPCM-Codierung von Fernseh-Signalen, Frequenz, Bd. 36, A. 6, Juni 1982, S. 161～168.

[3] 张春田，轮廓自适应预测的帧内 DPCM 图象编码，通信学报，第4卷 (1983年)，第1期，第1～7页.

[4] 徐孟侠，开关型自适应帧内 DPCM 图象编码，通信学报，第5卷 (1984年)，第1期，第7～18页.

[5] Cohen, P., Adoul, J. P., Adaptive Differential Coding of Picture Signals based on a Local Contour Prediction, NTC 76, Vol. 1, 6.1～1～5, Dec. 1976.

[6] Zschunke, W., DPCM Picture Coding with Adaptive Prediction, IEEE Tran. Commun., Vol,. COM-25 (1977), No. 11, pp. 1295～1302.

[7] Yamada (山田), K., Kinukaba, K., and Sasaki, H., A DPCM Coder Using Adaptive Prediction for TV Signals, ICC 77, Conference Record, Vol 1, 4 B. 1, pp. 76～80, 1977.

[8] Girod, B., Adaptive Prediction for DPCM Coding of TV Signals, IEEE Trans. ASSP, Vol. ASSP-29 (1981), No. 6, pp. 1142～1147.

[9] Heiss, R., Vorstellung eines neuen Adaptiven Intraframe-Pradtionsverfahrens, Forschungsbericht Nr. 112, Inst. f. Über-tragungstechnik und Electroakustik, Technische Hochschule Darmstadt, April 1983.

[10] 赵新建，图象信号的自适应变系数 DPCM 编码，通信学报，第4卷 (1983年)，第4期，第75～79页.

[11] 徐孟侠，帧内二维 DPCM 图象编码的一次实验，通信学报，第5卷 (1984年)，第4期，第58～61页.

[12] Pirsch, P., A New Prediction Design for DPCM Coding of TV Signals, ICC 80, Conference Record, Vol. 2, 31.2.1～5, June 1980.

[13] Connor, D. J., Pease, R. F. W., Scholes, W. G., Television Coding Using Two Dimensional Spatial Prediction, Bell Syst. Tech. J., Vol. 50 (1971), No. 3, pp. 1049～1061.

[14] CCIR Recommendation 500, CCIR 13 th Plenary Assembly, Vol. 11, pp. 65～68, 1974.

[15] 姚庆栋、顾伟康、徐胜荣、章守苗，电视信号的自适应全数字化综合高频编码，通信学报，第3卷 (1982年)，第2期，第8～16页.

[16] 王兆华，用二维 Walsh 函数分析彩色全电视信号，通信学报，第2卷 (1981年)，第2期，第50～57页.

[17] Wang Zhaohua, Theoretical Analysis and Experimental Investigation of the Two-Dimensional Spectrum of a PAL Composite Video Signal, ntz Archiv, Band 5 (1983), H. 5, S. 143～149.

[18] 王兆华，H. Amiri，二维低通列率重量数字滤波器的研究，通信学报，第6卷 (1985年)，第2期，第84～88页.

[19] 郑树德、范树香、毕厚杰，线性 DPCM 的误码响应分析，通信学报，第5卷 (1984年)，第4期，第47～53页.

[20] 肖自美，一种自适应压扩量化的电视信号帧内 DPCM 编码方法，1984年中国通信学会第五次图象通信年会论文集.

A FFT ALGORITHM FOR WIENER IMAGE RESTORATION

[Text] An algorithm using FFT for fast Wiener Image restoration by replacing the signal Teoplitz correlation matrix with circulant matrix is presented. This algorithm provides a computational reduction nearly from 4 to 1 as compared to that in (1). The restoration error of approximation has been evaluated and this Wiener Image restoration method has been studied experimentally.

REFERENCES

[1] William K. Pratt and Faramarz Davarian. Fast Computational Techniques for Pseudoinverse and Wiener Image Restoration, IEEE Trans. on Computers, Vol. C-26, No. 6, June 1977, pp.571—580.

[2] Andrews, H. C. and Hunt, B. R. (1977), Digital Image Restoration, Prentice-Hall, Englewood Cliffs New Jersey.

[3] Gonzalez, R. C. and Wintz, P. (1977) Digital Image Processing, Addison-Wesley, Reading, Massachusetts.

SINGLE BOARD COMPUTER BASED OPTIMIZATION OF SINGLE OUTPUT COMBINATIONAL LOGIC FUNCTIONS

[English abstract of article by Yan Zhenxiang [0917 2182 4382] of the Department of Automatic Control Engineering; paper received 8 November 1984]

[Text] This paper discusses implementation of optimization of single output combinational logic functions using single board computers. Features of the developed program are less superfluous items by improving the covering method and less memory capacity requirement by using machine-language and careful programming. The firmware of this program is able to solve many practical problems so that it can be used as a useful tool for logic design or an interesting practice for teaching purpose.

REFERENCES

[1] 刘明业：《数字系统计算机辅助设计》，国防工业出版社，1980年12月，第31~53页。

[2] 沈嗣昌：《计算机辅助逻辑综合》，高等教育出版社，1982年7月，第28~60页。

[3] Carroll, C. C.: A Fast Algorithm for Boolean Function Minimization, Technical Report, No. AU—T—3 AD680305, Dec. 1968.

/6091
CSO: 4009/1114

A PROGRAMMING TOOL TO SUPPORT STEPWISE REFINEMENT

[English abstract of article by Dong Yisheng [5516 6654 3932] and Wang Jing [3076 0513] of the Department of Computer Science and Engineering; paper received 24 November 1984]

[Text] An interactive programming tool, SPA, was presented. With the help of the tool, the stepwise refinement method can be applied easily to develop a program and generate a program text. The generated text is clear and readable with the comments which consist of development history and with the indentation format. A note facility contained in the SPA can be used to declare any entity which appears in the development process, so that the resulted program is executable immediately.

This tool, written in C, has been implemented in the MC68000 system on the UNIX. It is applicable to generate any program written in C, PASCAL and other structured programming languages.

REFERENCES

[1] Wirth. N.: Program development by stepwise refinement, Communications of the ACM, 14(4), 1971, 221—227.

[2] INCE, D. C.: A software tool for top-down programming, Software, 13(8),1984, 687—695.

[3] Teitelbaum, T. and Reps, T.: The cornell program synthesiser: A syntax-directed programming environment, Communictions of the ACM, 24(9),1981, 563—573.

[4] Bassett, P. and Giblon, J.: Computer aided programming, proceedings of the Conference on Software Development Tools, Techniques, and Alternatives, 1983, 9—20.

A UNIFIED SOLUTION OF CL FORMULA FOR INTERSECTION POINTS AND ITS APPLICATION TO MICROCOMPUTERS

[English abstract of article by Shen Kangle [3088 1660 2867] and Zhou Guangsheng [0719 1639 3932]; paper received 7 January 1985]

[Text] CL formula is established on the basis of circle beam transformation theory. It is applied to the calculation of intersection point co-ordinates for two dimensional pattern. The problem which was previously solved with a special technology can be transformed into a general solution only by a couple of normal vectors. It employs a unified CL hexagonal mode in order to favour memorization and computation. It can automatically operate in microcomputers as a mathematic model of dialogue NC auto-programming system. The sub-program can fully be used in its software system, thus decreasing storage capacity.

It is characterized by analyzing input parameters and determining the location of normal vector. This method fully conforms to CL hexagonal mode and can greatly enhance the speed of calculation, for its operation is simple and easy.

REFERENCES

[1] 沈康乐: CL公式的理论基础,《南京工学院学报》, 1983年第 4 期。

[2] 沈康乐、周广生: CL二元公式在 CROMEMCO 微型机上的使用,《广东机械》, 1983年第 2 期。

[3] 沈康乐、周广生: CL三元公式在微型机上使用,《机械开发》,1984年第 2 期。

[4] 沈康乐、周广生: CL非圆公式在微型机上的使用,《机械开发》,1984年第 3 期。

/6091
CSO: 4009/1114

BOUNDARY ELEMENT METHOD (BEM) IN ELECTROMAGNETIC POTENTIAL FIELD

[English abstract of article by Wu Wanchun [0702 8001 2504] and Liang
Changhong [2733 2490 3163] of Northwestern Telecommunication Engineering
Institute; paper received 20 February 1984]

[Text] Boundary Element Method (BEM) is a new numerical analysis method
presented recently by C.A. Brebbia et al. and it has been applied in
elasticity and other mechanical problems. The BEM is generally regarded as
a special case of weighted residual method (WRM), thus both accurate and
stable numerical results are expected. The BEM has the principle advantages,
namely smaller computation contents and more flexible for application over
subdomain method, such as finite element method, etc.

The BEM in electromagnetic potential field is considered. Various solutions
of Dirichlet, Neumann and Mixed boundary value problems are discussed. It is
seen that [H] in the BEM equation is a singular matrix. Hence the solution
of Neumann problem has an undetermined constant, it is known to be reference
potential.

Analytic formulations of matrix elements for constant elements and linear
elements are derived. More computation time is saved than a 4-point Gauss
quadrature rule by Brebbia.

Some examples showing the application of the BEM to two-wire transmission
line and a set of general computer programs are given.

REFERENCES

[1] M. A. Jaswon, Integral Equation Methods in Potential Theory I, Proc, Royal soc, (a), p. 275, 1963.
[2] J. L. Hess and A. M. O. Smith, Calculation of Potential-Flow about Arbitrary Bodies, In Progress in
     Aeronautical Sciences, Vol. 8, Pergmon Press, 1967.
[3] T. A. Cruse, Mathematical Foundations of the Boundary-Integral Equation Method in Solid Mechanics,
     Pratt and whitney Aircraft Group, Special Scientific Report, 1977.
[4] C. A. Brebbia, The Boundary Element Method For Engineers, Pentech Press, 1978.
[5] C. A. Brebbia, Boundary Element Techniques in Engineering, Newnes Butterworths Press, 1980.
[6] R. F. Harrington et. al, Computation of Laplacian Potentials by an Eguivalent Source Method Proc IEE,
     Vol. 116, No. 10, Oct. 1969. pp. 1715~1720.
[7] 杨乃恒，矩量法求解任意截面 TEM 传输线的特性阻抗，1983 年南京微波会议论文。
[8] 哈林登，正弦电磁场，上海科技出版社，1961。
[9] M. A. R. Gunston, Microwave Transmission-Line Impedance Data, VNR, London, 1972.
[10] 林为干，曾令濡，椭圆外导体—矩形内导体同轴线的特性阻抗，物理学报，第 30 卷，第 1 期，1981。
[11] 吴万春等，解任意截面形状传输线的边界元法，西北电讯工程学院院刊，第三期，1984。

/6091
CSO: 4009/1120

FAULT DETECTION AND DIAGNOSIS OF T-S-T DIGITAL SWITCHING NETWORKS

[English abstract of article by Chen Junliang [7115 0193 0081] of the Beijing Institute of Posts and Telecommunications; paper received 2 March 1984]

[Text] Algorithms for fault detection and diagnosis of T-S-T digital switching networks are devised. The main idea is to partition the whole network into basic modules and perform fault detection or diagnosis for a single basic module while the remaining part of the network is still able to perform switching functions normally. This paper assumes that there is only one faulty T switch or S module in a basic module, but multiple faults of different types are allowed to occur simultaneously within the faulty switch or module. The location of the faulty T switch or S module can be precisely determined by using the algorithm presented in the paper. The cost of fault detection in a basic module is $(3\ (2+\lceil (\log_2 N)/b-1\rceil),\ 12\ N + 4\ r)$, and the cost of fault location is $(5\ (2+\lceil (\log_2 N)/b-1\rceil),\ 14\ N + 4\ r)$. The first term in the formula represents the number of frames of test signals while the second term represents the number of words in the control memories necessarily to be rewritten during fault detection or location. N is the number of time slots, r is the number of T switches in the first stage of the T-S-T network and b is the number of binary digits in a time slot.

REFERENCES

[1] J. C. Bellamy, Digital Telephony, John Wiley & Sons, 1982.

[2] 顾重威，FETEX-150 程控数字电话交话机，电信快报，No, 4, 1982, pp 25～31.

[3] T. Yasui, T. Egawa, T. Sato, System Architecture of Digital Local Switching System, Review of the Electrical Communication Laboratories, Vol. 31, No. 1, Jan. 1983, pp. 16～23.

[4] 陈俊亮，数字交换网络中 T 及 S 接线器的模型与分析，《通信学报》第 6 卷第 3 期，第11～18页.

[5] 鲁刚，时分接线器的一种测试算法，北京邮电学院 1983 年学术讨论会论文，1983.

/6091
CSO: 4009/1120

ANALYSIS OF ANALOGOUS SIGNALS AND SYSTEMS BY USING GENERALIZED FUNCTIONS

[Text]   In this paper a method for analysis of analogous signals and systems
by using generalized functions is proposed. Signals are expressed by using
a generalized basis. Convolutional operation is converted to formal algebraic
operation. Electrical elements and systems are described by using convolution
equations and generalized equivalent circuits. Both zero-state solution and
zero-input solution are derived directly. This proposed method is more
systematized and profound than the popular time domain method and has wider
applicability than the transformation method.

REFERENCES

[1] J. Mikusiński, Operational Calculus, Pergamon Press.. 1959. (算符演算，王建午译， 上海科学技术出版社，
1964).

[2] A. Erdélyi, Operational Calculus and Generalized Functions Holt, Rinehart & Winston, New York,
1962.

[3] N. Balabanian, T. A. Bickart, Electrical Network Theory, John Wiley & Sons, Inc. 1969.

RESEARCH ON FOUNDRY COKE AND IMPROVEMENT OF CUPOLA MELTING QUALITY

[English abstract of article by the Cast Iron Melting Research Section, Shenyang Research Institute of Foundry]

[Text]   The authors have studied the regularity of bed coke combustion and melting process in cupola by using foundry coke developed recently in China, gas coke, and furnace coke respectively. In this paper, the characteristics of bed coke combustion and cupola melting effectiveness resulting from cokes of different qualities are compared. Influences of some coke properties, such as ash content, fixed-carbon content, sulfur content, strength, porosity, and reactivity etc. on the bed coke combustion and melting result are especially investigated in detail. The causes of obtaining high quality, high temperature molten iron by using foundry coke are analysed. It is indicated that Zhenjiang foundry coke is rather good and applicable to cupola melting process. The results show that Zhenjiang foundry coke improves the bed combustion process in the cupola, i.e., both the temperature and CO_2 distribution curves move towards the right and the high temperature region moves downward, the temperature and CO_2 content go down gently after reaching the maximum value, and CO_2 content at the charging opening is high whereas CO content is low. Thus, high quality, high temperature molten iron can be obtained with significantly economical benefit.

REFERENCES

〔1〕沈阳铸造研究所《开发铸造用焦论证方案》1983 年 2 月

〔2〕鞍山热能研究所、无锡柴油机厂 "铸造焦 研 制及应用的
    初步试验" 《铸造》1983年第 2 期

〔3〕铸造焦试验小组（天津拖拉机厂）《铸造焦 试 验总结》
    1983年 2 月.

〔4〕沈阳铸造研究所 刘幼华 "冲 天 炉测 试 方 法" 《铸工》
    1978年第 1 期。

〔5〕南京工学院周重光《倒置大排距双层送风冲天炉 》

〔6〕西安交大陆文华主编《铸铁及其熔化》1981年

〔7〕东北工学院等校编《铸铁及其熔化 》

〔8〕马利延巴赫（苏）《冲天炉工作的强化》1956年

〔9〕《炼焦化学》1982年第 1 期.

〔10〕《铸研报告》（日）1962年 №16.

〔11〕J.E.Rshdor "冲天炉燃料 述评" 《Faundry M.T.》
    1981.2.

〔12〕J.P.Graham等 "焦炭块度和性能对冲天炉操作的影响"
    《The British Foundryman 》1962年 5 月

DEVELOPMENT OF TYPICAL CASTING TECHNOLOGY DESIGN USING COMPUTER

[English abstract of article by Zhao Jian [4392 0256], Zhang Yi [1728 3015], and Zhang Jiaqiu [1728 0163 4428] of Shenyang Research Institute of Foundry]

[Text] Technology design plays an important part in foundry production. For many years, a lot of foundry researchers have been eager to find a method to make it accurately and quickly. Based on the experiences of practical production, the authors have developed a software of designing casting technology by using computer. This paper describes in detail the general principle and the operating method of this software.

/6091
CSO: 4009/1121

ANALYSIS OF LASER SCANNING SYSTEM

[Article by Qiu Jinhui [6726 6930 6540], Institute of Lasers, Fujian Normal
University]

[Abstract] This paper analyzes the parameter relations of a scanning system,
the distortion property of the scanning lens, and the performance of mechani-
cal deflectors using gaussian light-beam theory in order to solve problems in
system design. A laser-scanning system placed in front of an objective lens
is used in research involving planar scanning of a large visual field. The
basic components of the system are a mechanical deflector and a scanning lens;
its main requirements are high resolving power (the number of light spots
distinguished) and a uniform scanning rate. The system's general index is
the product of velocity and capacity, the resolving power. Three figures
show the laser-scanning system, distortion property of the scanning lens, and
a rotating multifacet lens deflector. A total of 23 mathematical equations
are derived in describing the distortion property and two types of mechanical
deflectors. The paper was received for publication on 3 February 1986.

THREE-PHASE CURRENT STABILIZING, CHARGING PULSED POWER SUPPLY FOR SOLID STATE LASERS

[Article by Yang Weirong [2799 5898 2837], Yin Hua [3009 7520], and Zhang Zhaodi [1728 2156 1229], Shanghai Institute of Laser Technology]

[Abstract] The paper describes a new pulsed power supply, using a three-phase current-stabilizing charging device for solid state lasers with an efficiency of 50-80 percent and a charging accuracy of higher than 99 percent. The power supply system can withstand an output short-circuit current of about 1 A. Its output voltage can be varied from zero to the maximum required value and a storage condenser can be easily changed at the operator's discretion. Its size is about 0.4 m^3, with a maximum power output of 3 kW. Composed of three-phase type E reactors, the power supply system applies the LC transformer technique to convert a constant-voltage power source to a constant-current power supply. Six figures show the system's operating principle, circuits of the three-phase LC transformer, the transformer's input-output property test arrangement, its AC and DC output performance curves, and its current input performance curve. The paper was received for publication on 21 January 1986.

10424/6091
CSO: 4009/102

EXPERIMENTAL RESEARCH ON STIMULATED RAMAN EFFECT--SOURCE OF ULTRAVIOLET LIGHT FOR VITAMIN D SYNTHESIS

[Article by Zhao Zhensheng [6392 7201 5116], Anhui Institute of Optics and Fine Mechanics, Chinese Academy of Sciences, and D. Proch, Max-Planck-Institut fur Quantenoptik, Gauching, West Germany]

[Abstract] To obtain a UV-optical source for vitamin D synthesis, the authors studied stimulated Raman scattering (SRS) of different media with Raman wavelength varying between 280 and 300 nm and calculated the related parameters by using a discharge-pumped TEA KrF excimer laser (248 nm). As shown in a figure, the KrF laser has a discharge volume of $60 \times 5 \times 3$ cm^3 and a concentrated capacitance of about 50 nF. When discharged to 30 kV, the thyratron-controlled (pre-ionization) TEA device begins to discharge. The resonant cavity is composed of aluminum-coated completely reflected and quartz planar lenses; the laser's output pulse energy is 250 mJ. Three other figures show the experimental arrangement, energy relationship between pumped laser and the Stokes displacement, and the increase in SRS intensity with an increase in CH_4 gas pressure. Two tables show the selected Raman media pumped wavelengths for vitamin D synthesis and Raman scattering cross-sections of some molecules. The paper was received for publication on 20 December 1985.

10424/6091
CSO: 4009/102

MYCOFLORA IN NATURALLY FERMENTED CHINESE SAUCES IN BEIJING AND THEIR ASSAY OF AFLATOXIN B1

[Text] The distribution of mycoflora in naturally fermented sweet flour paste, and salted fermented soya paste, in Beijing region were surveyed. A total of 12 genera, 30 species of fungi were isolated from the sweet flour paste. The predominant fungi were Chlamydomucor sp., Aspergillus flavus and Penicillium chrysogenum. In salted soya paste 18 genera, 37 species of fungi were isolated, in which Aspergillus flavus predominated.

Aflatoxin B1-producing ability of the strains of Aspergillus flavus were assayed. In fermented sweet flour paste among the 128 strains of Aspergillus flavus, only one was found to be positive. Among the 19 strains of Aspergillus flavus isolated from salted soya paste one positive strain was encountered also. But no aflatoxin B1 was detected in mature pastes.

REFERENCES

1. 冀鹤鸣. 西北酱曲中曲菌之研究. 黄海发酵与菌学特辑 1948; 10:40.

2. 刘守初. 北京酱曲中曲霉的检查. 黄海发酵与菌学特辑 1950; 11:150.

3. Hara S, et al. Aflatoxin-producing strains of *Aspergillus flavus* detected by fluorescence of agar medium under ultraviolet light. Microbiol Appl 1974; 27:1118.

4. 张国柱，等. 发酵菌种黄曲霉毒素B1的测定和AS 3.870 菌株的鉴定. 微生物学通报 1981; 8:216.

5. 孟昭赫，等. 真菌毒素研究进展. 北京：人民卫生出版社, 1979:156—173.

6. 一岛英治. 麹菌类に関する研究からみた日本の醸酵学 (II) マイコトキシンの生化学. 醸酵協会誌 1970; 28: 482.

7. 真锅胜ろ. 醸酵食品中の蛍光成分に関する 研究(第2報) みそおよびみそ麹のアフラトキシン汚染の有無につい て. 日本食品工業学会誌 1972; 19:76.
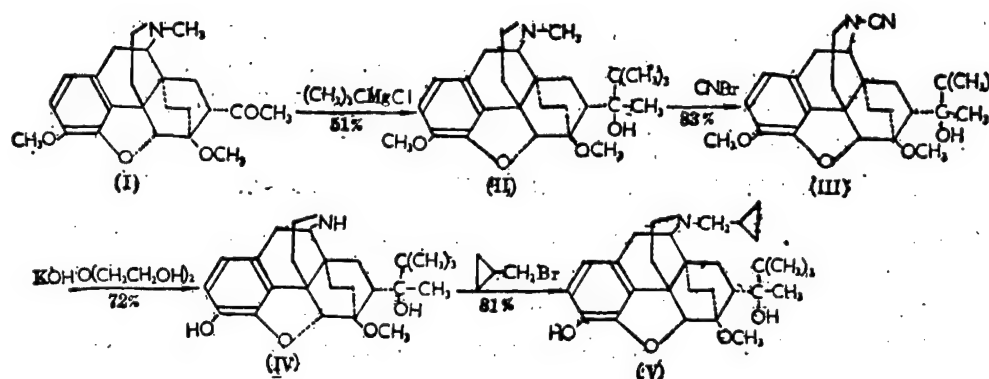
8. 居乃琥. 黄曲霉毒素. 北京：轻工业部出版社, 1980: 219—294.

/6091
CSO: 4009/1107

SYNTHESIS OF THE HIGHLY POTENT ANALGESIC, BUPRENORPHINE

[English abstract of article by Wan Weiqin [8001 4856 0530], Qiu Zhuibai
[0092 4856 4102], Zhou Youjun [0719 2589 7486], and Huang Qiang [7806 1730]
of the Department of Medicinal Chemistry, School of Pharmacy, Shanghai
Medical University, Shanghai]

[Text] The highly potent analgesic, "buprenorphine," has been successfully
synthesized with a new improved method which eliminates N-methyl and O-methyl
simultaneously, replacing Bentley's two-step reaction. In addition to
simplification of procedures, this new method also raised the total yield
from 5.06 percent to 20 percent, making industrial production of buprenorphine
possible.

REFERENCES

[1] Mogens K, et al:A Compartive study of intramuscular Buprenorphine and Morphine in the treatment
of chronicpain of malignant origin. Br J Clin Pharmacol 1982 13:457

[2] Bentley KW: Thebaine and oripavine derivatives. Br Patent 1968:1136314

[3] 张明立等: 强效镇痛药 Buprenorphine 的合成。医药工业 1983(2):6

[4] 万维勤等: 阿片受体拮抗剂特培诺啡的研制。上海第一医学院学报 1985 12(1):25

[5] 刘懋勤等: 吗啡拮抗剂——纳洛酮的合成。医药工业 1980(3):1

[6] Bentley KW, et al:Novel analgesics and molecular rearrangements in the morphine-thebaine group
III. Alcohols of the 6,14-endo-ethenotetrahydrooripavine series and derived analogs of N-allyl-
normorphine and norcodeine. J Am Chem Soc 1967 89:3281

[7] Michael PK, et al:Analgesic narcotic antagonists I. 8β-alkyl, 8β-acyl, and 8β-(tertiary alcohol)
dihydrocodeinones and dihydromorphinones. J Med Chem 1980 23(2):173

/6091
CSO: 4009/1113

DESIGN CRITERIA OF PWR FUEL ASSEMBLY

[Article by Tian Sheng [3944 4141] and Cheng Rongzhen [4453 5554 3791]]

[Abstract] The article presents the design criteria of fuel assemblies for a pressured water reactor (PWR) in a nuclear power plant; the criteria (design standards) are briefly explained. The functioning, use conditions, and properties of the fuel assembly should be considered in specifying the design criteria, which are only adaptable to the fixed-type PWR fuel assembly using a zirconium-tin alloy to make shell-enclosed tubes and uranium dioxide for the fuel cores. The criteria only stress which design requirements should be satisfied, not how to satisfy these requirements. The criteria serve only for design problems related to nuclear, heat-power, and hydraulic aspects. In addition, an appendix lists the design working conditions of PWR power plants with four levels of possible accidents described. Three tables list the limits of allowable-stress values and austenite (and zirconium-tin alloy) components.

10424/6091
CSO: 4009/104

RELIABILITY ANALYSIS OF A NEW PROTECTION SYSTEM FOR THE SWIMMING POOL REACTOR

[Article by Meng Fanshu [1322 4907 3219]]

[Abstract] The paper presents a new protection system for the swimming pool reactor; the system consists of HTL integrated circuits. The system has redundancy in its design, characterized by a coincidence logic two-out-of-four (2/4). A fault tree analysis is used to evaluate system reliability. The analysis is examined to the extent of "low flow of primary coolant" relying on logic circuits. The author constructed two fault trees: "failure to scram" and "spurious scram." System reliability is higher than the allowable safety indexes. Ten figures show the protection system, LD logic circuits for protective passages for scram events, an electromagnetic driving circuit, fault trees for system (and module M) scram, a simplified scram fault tree, and a simplified sub-fault tree. Two tables list the system's minimum cutoffs and data on fault rates.

INVESTIGATION AND TESTS FOR CONTINUOUSLY IRRADIATING SHORT-LIVED ISOTOPES IN HFETR

[Article by Shan Runhua [0830 3387 5478], Zhang Dehe [1728 1795 3109], Zhao Xihou [6392 6932 0230], Li Manchang [2621 3341 2490], Lu Changlong [7627 7022 7893], and Li Yinsheng [2621 6892 3932]]

[Abstract] The grid elements of the high flux engineering test reactor (HFETR) are utilized to install $\phi 63$ pressured tubes filled with ion-free water. MoO_3 irradiating powder (sealed in glass tubes) is placed in pressured tubes to produce short-lived isotopes. This is a new application of HFETR utilization. Using MoO_3 irradiation as an example, the paper describes the continuous irradiation test with the production of $^{99m}Mo-^{99m}Tc$ isotope. Also described are the installation types, test results, and production capacity. Seven figures show an irradiating assembly, its lateral cross-section, changes in the ^{99m}Mo scale with irradiation time and reactor output power, the correlation between reactor output power and irradiation days by irradiating 3-C/g molybdenum isotopes, and the lateral cross-section of irradiation layouts with different isotope target pieces. Six tables show changes in irradiation time (and reactor output power) with ^{99m}Mo, irradiation days required for different reactor power ratings in producing a 3-C/g molybdenum isotope, irradiation times required at different operating power ratings (of the reactor) for producing a 3-C/g molybdenum isotope, effective cross-section areas of filling with the MoO_3 powder in three layouts, and the total filling capacity of molybdenum in the three layouts.

STRESS MEASUREMENT OF TiN THIN FILMS

[Article by Wang Yinghua [3769 5391 5478] and You Yinjuan [1429 1714 1227] of Engineering Physics Department, Qinghua University]

[Abstract] For the case of a TiN ionic coating layer, approximately 0.2-0.3 μm thick, no x-ray diffraction curves can be detected using conventional diffraction instruments. The authors employed the baseline-segment method and the edge inclination method to determine stresses in the above-mentioned coating layer. Two figures show the principle of stress measurement in the edge inclination method and determination results for Cu crumb-samples. Two tables list stress data for the TiN coating layer determined with the edge inclination method and results from using the baseline-segment method. From these data, the authors drew the following preliminary conclusions: (1) For thin films not exhibiting x-ray diffraction curves, the baseline-segment method can be applied to estimate the stress variation law of thin films; and (2) for thin films with a low-incidence angle, stress determination is feasible using the edge inclination method and stress estimation--with the baseline-segment method. Zhang Chun [1728 4783] of Nuclear Energy Institute, Qinghua University, provided samples used in the experiments; Xu Kesheng [6079 0668 0524] and Chang Baoliang [1603 0202 5308], both students at the university, conducted much of the work in setting up the stress-testing methods. The authors are grateful to these individuals.

IMPROVED K VALUE METHOD IN MULTIPHASE QUANTITATIVE DIFFRACTION X-RAY ANALYSIS

[Article by Yang Zhuanzheng [2799 0278 6927] and Zhong Fumin [6945 4395 3046] of Shanghai Institute of Metallurgy, Chinese Academy of Sciences]

[Abstract] F.H. Chung proposed the K value method in the x-ray quantitative analysis method in ADVANCED X-RAY ANALYSIS, Plenum Press Vol 17 (1973), p 106, and J. APPL. CRYST. No 7 (1974), p 519. The method has been widely used; this paper presents its principle. The only table in the paper lists the relative errors of the experimental results. A larger deviation appears only in the Si relative errors in one of three test specimens. The error depends on the random orientation and heterogeneity of the original and reference specimens as well as on the precision of the strength determination. Compared with the internal index method and increment method, the K value method is much simpler in experimental procedures, not requiring that standard specimens be added to the unknown specimen. The K value ratio can be derived from a reference specimen of a known weight fraction. Thus, the error sources are fewer.

RESEARCH FRONTIER IN ATOMIC PHYSICS--DYNAMICS OF EXCITED ATOMS AND MOLECULES

[Article by Li Jiaming [2621 1367 2494], Institute of Physics, Chinese Academy of Sciences]

[Abstract] Collisions of atomic nuclei lead to submicroscopic energy transfers owing to the production of excited atoms or molecules with prolific species and combinations. These excited atoms or molecules can be regarded as intermediate complexes of the atomic collision processes. Exploring the structure of the excited state of atoms and molecules is a problem in the quantum multibody dynamics of long-range coulombic interaction. Progress in experimental techniques has made it more convenient to observe the excited states; in addition, the effects of magnetic and electric fields on the excited atoms and molecules can be explored. Six figures show a high-resolution laser spectrum of excited atoms, electron energy-loss spectrum of HF molecules, ionized energy spectrum of the vacuum ultraviolet wave band, absorption spectrum of threshold values and its atomic neighborhood, the relationship between orbital energy and interatomic distance, and the near-threshold structure of electrons. The author is grateful to the support of the Chinese Academy of Sciences and China Natural Science Fund for this research.

PROGRESS IN HIGH-ENERGY PHYSICS

[Article by Zhu Hongyuan [2612 3163 0337], Institute of High-Energy Physics, Chinese Academy of Sciences]

[Abstract] Since the accelerator energy exceeded 1 GeV in the early 1950's, it has been feasible to study the phenomena of high-energy physics systematically. In atomic studies, quantum mechanics and quantum electromechanics laid the foundation for the quantum field theory, the basis of present-day particle physics, another name for high-energy physics. Both quantum mechanics and quantum field theory have the following fundamental principles: (1) the values of a physical quantity can be discontinuous, and (2) the physical state obeys a statistical law. Physical phenomena still obey the fundamental law of quantum theory, though experimentally the submicroscopic exploration has advanced from 10^{-8} cm to 10^{-16} cm, and energy has been increased from several electron volts to hundreds of billions of electron volts. The wealth of experimental data can lead to theoretical breakthroughs only with profound understanding such as Niels Bohr's insight in pioneering the quantum theory. Two tables show the regularity of particle properties and the total cross-sections of three high-energy collision processes, determined by strong and weak interactions, as well as by electromagnetic interactions.

10424/6091
CSO: 4009/93

CONDENSED-MATTER PHYSICS IN THE EIGHTIES

[Article by Xie Xide [6200 1585 1795], Fudan University]

[Abstract] In recent years, a diversity of research entities is one of the features of advances in condensed-matter physics: from simple to complex crystal structures. Three other features are: use of modern experimental apparatus (ultra-low temperatures, high pressures, high-power lasers, magnetic resonance, electron beams, and ion beams), penetrating theoretical research, and a close relationship with computational physics. The advent of the computer is pushing theoretical and experimental analyses to a new stage. The physical phenomena and research areas stressed in the eighties are: quantum Hall effect and fractional quantum Hall effect, energy-gap engineering, polyethine and other electrically conductive polymers, organic superconductors, heavy fermions, and five-axis symmetry—quasi-periodicity (or quasi-crystal). Fifteen figures show the quantum Hall effect, the effect obtained by varying the magnetic field, the effect observed in a heterogeneous junction with a very high magnetic field and at a very low temperature, the relationship between electron transfer rate and temperature in a hetero-potential well, bias photoelectrons and cavity ionization doubling of avalanche diodes, the parabola-type effective well potential of the elongation of molecular beams, the relationship between photoconductivity and time of super-crystal lattice, A and B phases in trans- and cis-polyethine, transitions between A and B phases (and vice versa) in polyethine, attraction and rejection between electrons, comparison of resistivity-temperature relationship of organic superconductors and other materials, the basic elements that make up organic conductors and organic superconductors, the structure of $(TMTSF)_2PF_6$, the relationship between resistivity and temperature for heavy fermions, an electron diffraction diagram of Al_6Mn alloy particles, and a brick-laying diagram after Penrose. Two tables list data for heavy fermion parameters and its Wilson ratio.

NEW NONLINEAR OPTICAL CRYSTAL KTP

[Article by Huang Zhao'en [7806 2600 1869], Institute of Artificial Crystals, State Bureau of Construction Materials Industry]

[Abstract] The recently discovered nonlinear optical crystal $KTiOPO_4$, KTP for short, exhibits valuable properties for use with lasers: a high non-linear coefficient, phase matching at room temperature, insensitivities to changes in temperature and angle, transparency in the range between 0.35 and 4.5 µm, high threshold value (greater than 300 MW/cm^2) to damage, good machinability, stability of chemical properties (such as immiscibility with moisture and tolerance of high temperature), and capability of growing large crystals with satisfactory (optical) homogeneity. Rarely does a crystal exhibit simultaneously as many advantages as KTP does; it has good strategic significance in its applications in bluish green lasers, which in turn may initiate nuclear fusion and is a basic weapon in the SDI (Strategic Defense Initiative) program. KTP's importance in peace and war led to strict controls on its export from the United States. Currently there are two KTP growth methods: water-heating method and fused-salt method. The structure of KTP is explained in the projection of an ATP crystal cell along the [010] direction shown in a figure. Three other figures show the relationship between refractive index and wavelength of KTP, the stereographic projection of phase-match loci caused by a second harmonic wave due to interaction of two KTP types, and the relationship between incident power density and an energy conversion efficiency of double frequency.

MAGNETIC FLUIDS AND THEIR APPLICATIONS

[Article by Guo Huacong [6753 5478 5115], Institute of Nuclear Science and Technology, Sichuan University]

[Abstract] A magnetic fluid is a highly magnetic colloid with a stable distribution of magnetic particles (for example, Fe_3O_4). The colloidal fluid does not aggregate and settle despite the action of gravity and magnetism. A magnetic fluid can be applied in a wide range of fields: sealing, separation by employing differences in specific gravities, jet printing, magnetic separation, lubrication, and magnetic recording as well as in bearings and attenuators. The paper goes on to describe the properties and production of magnetic fluids. Some banks in the United States utilize checks printed with magnetic ink in computer processing. Magnetic fluid can also be used to convert heat energy directly into mechanical energy as well as be used in waste water treatment. Recently in Japan, a patent was granted for a cobalt-iron magnetic fluid with saturated magnetizability intensity as high as 2,460 gauss. Two figures show potential-energy curves of two magnetic particles and the properties of a magnetic fluid. One table lists properties of magnetic fluids.

STUDY OF THE LASER ANNEALING OF THE BORON-DIFFUSED SILICON SINGLE CRYSTALS

[English abstract of article by Fan Depei [5400 1779 1014], Zhu Bing [2612 0365], and Chen Nandou [7115 0589 2435]; paper received 11 April 1983]

[Text] Laser annealing of (111) and (001) Si single crystal wafers by an electro-optically Q-switched Nd^{3+}:YAG laser were studied by X-ray divergent beam diffraction method and Van der Pauw method of Hall effect measurement. It is found that lattice constants contract about 2.2×10^{-3} and the concentrations of surface carriers have risen about an order of magnitude after laser annealing.

REFERENCES

[1] C.W.White. et al, Science 204, 461 (1979)

[2] R. T. Young. Appl. Phys.. Lett. 33, 14 (1978)

[3] B. C. Larson. Appl. Phys. Lett. 32, 801 (1978)

[4] 张杏奎等 激光 6，23 (1979)

[5] H. Yakowitz. "The Divergent Beam X-ray Technique" Advances in Electrons and Electron Physics suppl 6 p361 (1969)

[6] G. L. Pearson. J. Bardeen. Phys. Rev. 75, 865 (1949)

[7] 丘第荣、范得培、激光与红外 3，9(1981)

/6091
CSO: 4009/1116

APPLICATION OF A MICROPROCESSOR IN TEMPERATURE CONTROL

[English abstract of article by Ying Zhaomin [2019 2507 2404], Li Zhihua [2621
2535 5478], Ji Hong [1323 4767], and Ji Jiaben [1518 1367 2609]; paper received
2 September 1983]

[Text] Software and hardware of the microprocessor used for temperature
control is described. The temperature control system operates in the liquid
nitrogen temperature range from 70K to 90K. The stability of temperature
control is better than 10mK.

REFERENCES

[1] R.B. Strem, B.K.Das and S. C. Greer Rev, Sci instrum. Vol, 52,
     No11, Nov. (1981).

[2] J. P. Eisenstein, G. W. Swif and R. E Packard Cryogenics Nov.
     (1979) 666.

[3] A. Sawade, T. Mamiya, H. Fukuyama and Y. Masuda Cryogenics
     July (1982) 354.

/6091
CSO: 4009/1115   END